

Novel Optimal Trajectory Design in UAV-Assisted Networks: A Mechanical Equivalence-Based Strategy

Xiaopeng Yuan^{ID}, *Graduate Student Member, IEEE*, Yulin Hu^{ID}, *Senior Member, IEEE*,
Deshi Li^{ID}, and Anke Schmeink, *Senior Member, IEEE*

Abstract—Unmanned aerial vehicles (UAVs), also known as drones, have already been widely implemented in wireless networks for promoting network performance and enabling new services. To efficiently explore the diversity introduced by the mobility of UAV, many efforts have been made in the design of the UAV trajectory under various wireless scenarios. However, the continuity of a UAV trajectory in both time and topology forces researchers to approximate the UAV trajectory by a discrete model, which always results in a sub-optimal solution. To tackle the difficulty and obtain the optimal trajectory, in this work we introduce an artificial potential field (APF) to reformulate the objective in trajectory design, with which the UAV trajectory problem can be completely equivalent to a mechanical problem. In such mechanical problem, the UAV trajectory is represented by an extremely soft and thin rope with variable density carrying UAV speed information, and the original objective of optimizing the system performance is transformed to minimizing the overall artificial potential energy on the rope. As a result, the rope in the optimal solution stays in a state of equilibrium and the UAV trajectory can be equivalently optimized by designing the shape of a rope under the APF via mechanical principles. We provide a case study to describe in detail the problem equivalence, i.e., taking a single-user network as an example in which the throughput between UAV and the user is considered as the objective performance. In particular, the optimal trajectory of a UAV is constructed based on mechanical principles, while the global optimality is also rigorously proved and further confirmed via simulations. Moreover, we also highlight that the novel strategy of constructing equivalent mechanical problem has the possibilities to be extended to various UAV trajectory problems under different scenarios with different performance optimization objectives.

Index Terms—UAV, trajectory design, artificial potential field (APF), mechanical equivalence, equilibrium state.

Manuscript received October 21, 2020; revised February 16, 2021; accepted April 11, 2021. Date of publication June 14, 2021; date of current version October 18, 2021. This work was supported in part by German Research Council (DFG) Project under Grant SCHM 2643/16. (Corresponding author: Yulin Hu.)

Xiaopeng Yuan and Yulin Hu are with the School of Electronic Information, Wuhan University, Wuhan 430072, China, and also with the ISEK Research Area, RWTH Aachen University, 52074 Aachen, Germany (e-mail: yuan@isek.rwth-aachen.de; yulin.hu@whu.edu.cn).

Deshi Li is with the School of Electronic Information, Wuhan University, Wuhan 430072, China (e-mail: dsli@whu.edu.cn).

Anke Schmeink is with the ISEK Research Area/Lab, RWTH Aachen University, 52074 Aachen, Germany (e-mail: schmeink@isek.rwth-aachen.de).

Color versions of one or more figures in this article are available at <https://doi.org/10.1109/JSAC.2021.3088627>.

Digital Object Identifier 10.1109/JSAC.2021.3088627

I. INTRODUCTION

WITH their great flexibility, unmanned aerial vehicles (UAVs) have enabled enormous potential deployments in various domains, like cargo transport, environment monitoring, rescue assistance and mineral exploration [1]–[3]. Especially in wireless networks, the high mobility of UAVs helps to avoid the possible blockage in wireless signal transportation [4], [5] and to construct wireless channels with much higher quality, in comparison to those in traditional static networks [6]. To exploit these advantages, the static deployment position of UAVs has been carefully designed to raise the network performance, e.g., to enlarge the coverage for ground users while deploying UAVs as a base station [7]–[9] and to enhance the reliability of wireless connection while applying UAVs as a relay [10]. Moreover, also for wireless networks where UAVs have taken over communication tasks, the trajectory of a mobile UAV is optimized (predesigned before starting the tasks) aiming at maximizing the channel capacity [11]–[13], improving energy efficiency [14]–[17], and minimizing the total task completion time [18]. However, for such UAV trajectory (pre)design, a huge difficulty is that the trajectory is generally required to be continuous in both time and (the coordinates of the UAVs) location, i.e., an infinite number of variables needs to be optimized at the same time.

To deal with this difficulty, the most popular strategy in the literature is to approximate the continuous trajectory with a large number of discrete points while each two neighbour points are constrained by a maximum distance [13]–[18]. The trajectory is then **approximately** optimized by designing the positions of these discrete points. The obvious drawbacks of this strategy are: i. the resulted trajectory solution is sub-optimal, and ii. the accuracy of the approximation is an issue, while improving the accuracy significantly increases the complexity of the strategy. On the other hand, as another trajectory design strategy, a successive-hover-fly (SHF) structure is inserted in UAV trajectory [11], [12], [19], where the UAV is assumed to have hovering and flying behaviours, i.e., it successively hovers at different hovering points with different hovering durations. Following the SHF structure, the trajectory is designed via determining the positions of these hovering points and corresponding hovering durations. Nevertheless, this strategy only works for scenarios where the SHF structure

assumption of the UAV trajectory does not lose the optimality of the original objective of the design. In addition, although the complexity of the SHF-based trajectory design is significantly reduced in comparison to the popular approximation strategy, its optimality/accuracy is indeed sacrificed. This is due to the fact that the UAV is assumed to fly between hovering points along straight lines in an SHF structure. Hence, the optimality only holds for a one-dimensional (1D) special topology [19] and is definitely inaccurate for general scenarios where the UAV possibly flies via an arc/curve trajectory. To the best of our knowledge, the global optimal UAV trajectory has not been obtained or mathematically described in application scenarios with a general topology.

In this paper, we introduce a mechanical concept, namely the artificial potential field (APF), to the UAV trajectory design for a general UAV-enabled network with a general network topology. A completely novel strategy is proposed, in which we first represent the design objective and the UAV trajectory respectively by the APF and a physical rope with certain density carrying the information of the UAV speed. As a result, the UAV trajectory design problem is equivalently transformed to a mechanical problem minimizing the overall potential energy on the equivalent rope. Due to the fact that the rope must stay in a state of equilibrium when the overall potential energy is minimized [20], the UAV trajectory is optimally constructed by designing the rope shape based on the mechanical principles in equilibrium. In the following sections, the design strategy is first illustrated via a single-user example network, in which the throughput between UAV and user is considered as objective to be maximized. Then the global optimal trajectory is mathematically constructed. After that, we confirm the optimality of our proposed strategy in single-user network through simulations and highlight the abundant possible extensions of the novel strategy in UAV trajectory designs. The contributions of this paper are listed as follows:

- **Physical Equivalence of Trajectory Design:** In this work, we have proposed a novel strategy for UAV trajectory design. For the first time, the UAV trajectory design problem is completely equivalent to a physical problem with the assistance of APF. With the physical equivalence, the UAV trajectory design problem becomes analyzable and the optimal solution can be characterized via physical principles. The physical equivalence will definitely facilitate the analysis and characterization of various trajectory design problem.
- **Optimal Trajectory Solution for Single-User Network:** To clarify the novel strategy, we start with a single-user network. While targeting at maximizing the overall throughput between UAV and the user, we characterize the UAV speed in optimal solution and based on physical principles optimally constructed the optimal trajectory for UAV. Since most of the existing strategies for UAV trajectory design can only guarantee a suboptimal solution, our work with optimality has shown significant analytical contributions. Furthermore, the optimality has also shown to be able to be extended in single-user network with many complex models and objectives.

- **Closed-Form Trajectory Solution:** Beside of the optimality, for the first time, we also characterize the closed-form expression for the continuous optimal UAV trajectory. With the closed-form expression, the computational complexity for constructing the optimal trajectory is extremely lower. The extremely high efficiency will be much attractive in some latency-critical scenarios.

It should be mentioned and clarified that the concept of APF has been proposed in robot path design [21] and then extended to some UAV path designs [22]. However, in these studies, the APF has only applied as an approximation tool for the algorithms to approximately model the obstacles constraints, i.e., avoiding collisions on the path (not a trajectory containing the location and speed information at each time point), which does not introduce any mechanical significance on the APF. This is totally different from our proposed strategy which equivalently totally transforms the trajectory problem formulation to a mechanical one and obtains the optimal trajectory solution.

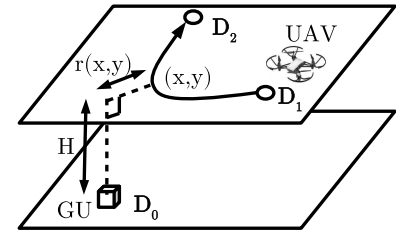
The rest of this paper is organized as follows. In Section II, we describe our considered example single-user network and formulate a UAV trajectory design problem aiming at maximizing the overall throughput. Next, the original problem is reformulated and completely equivalent to a mechanical problem in Section III. Then, we equivalently focus on the mechanical problem and construct the optimal solution for UAV trajectory in Section IV, which requires a design of an optimal initial tension. In Section V, we provided an approach for obtaining the optimal initial tension. Finally, the work is validated via simulations in Section VI and concluded in Section VII.

II. PROBLEM STATEMENT IN SINGLE-USER NETWORK

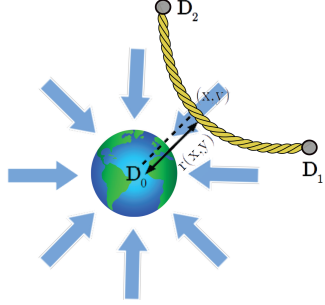
To present this novel UAV trajectory design strategy, we consider a single-user network as an example, where a UAV is deployed as a mobile base station as shown in Fig. 1(a). The user is placed at position $\mathbf{D}_0 = (w_{0,x}, w_{0,y})$ on the ground. The UAV is operated at a fixed altitude $H > 0$ being responsible for wirelessly communicating with the ground user (GU). The horizontal position of the UAV at time point $t \geq 0$ is represented by $(x(t), y(t))$, which is clearly a continuous function in time t . Moreover, the UAV is assumed to have a maximum speed limit V , i.e., $\|(\dot{x}(t), \dot{y}(t))\|_2 \leq V, \forall t \geq 0$. Further note that we consider a rotary-wing UAV. Since the flying speed of rotary-wing UAV can be generally adjusted in a very short time [14], [15], we assume the acceleration limit for UAV is ignored. We denote by T the communication time duration between the UAV and the GU, e.g., the duration could be allocated by a higher layer scheduler. Then, for any time point t on the interested UAV trajectory, we have $t \in [0, T]$. In particular, within this duration of T , the UAV is required to fly from a given starting point $\mathbf{D}_1 = (w_{1,x}, w_{1,y})$ to the given destination $\mathbf{D}_2 = (w_{2,x}, w_{2,y})$, as implied in Fig. 1(a), which implies that

$$(x(0), y(0)) = \mathbf{D}_1 = (w_{1,x}, w_{1,y}), \quad (1)$$

$$(x(T), y(T)) = \mathbf{D}_2 = (w_{2,x}, w_{2,y}). \quad (2)$$



(a) Trajectory design in single-user network.



(b) Rope equilibrium problem in a gravitational field.

Fig. 1. Examples of two kinds of problems.

We consider the scenario where $\|D_1 - D_2\|_2 = \sqrt{(w_{1,x} - w_{2,x})^2 + (w_{1,y} - w_{2,y})^2} \leq VT$ holds, otherwise the UAV is not capable of completing the flight from D_1 to D_2 within allocated time duration T , i.e., the trajectory design is infeasible. Note that it is reasonable to assume given starting and ending points for UAV trajectory design, since the UAV is generally responsible for multi-tasks in practice and for a certain task the starting and ending points highly rely on the previous and next UAV tasks.

We refer to the channel gain to represent the channel quality. We adopt to apply the free-space path loss model as in [23]–[25] due to the high probability of line-of-sight (LoS) between UAV and GU in short range [6]. The channel gain at time t is given by $h(x(t), y(t)) = \frac{\beta}{r(x(t), y(t))^2 + H^2}$, where β denotes the channel gain at a reference distant of $1m$ and $r(x(t), y(t))$ represents the horizontal distance from point $(x(t), y(t))$ to the GU at position D_0 , i.e.,

$$r(x(t), y(t)) = \sqrt{(x(t) - w_{0,x})^2 + (y(t) - w_{0,y})^2}. \quad (3)$$

For the wireless communication between the UAV and the GU, we denote by P the transmit power from the GU in the uplink scenario (or from the UAV in the downlink case). Therefore, the maximum transmission rate between the GU and the UAV at time t is formulated as

$$R(x(t), y(t)) = B \log_2 \left(1 + \frac{P}{\sigma^2} \frac{\beta}{r(x(t), y(t))^2 + H^2} \right), \quad (4)$$

where B represents the bandwidth and σ^2 is the noise power level. As a result, the corresponding total throughput over time duration T is given by

$$U(\{x(t), y(t)\}) = \int_0^T R(x(t), y(t)) dt. \quad (5)$$

Following the above system model, we aim at maximizing the throughput $U(\{x(t), y(t)\})$ by optimizing the UAV trajectory $\{x(t), y(t)\}$ under the maximum UAV speed limit V .

Thus, the original problem is described as

$$(OP) : \max_{\{x(t), y(t)\}} U(\{x(t), y(t)\}) \quad (6a)$$

$$s.t. \quad \|\dot{x}(t), \dot{y}(t)\|_2 \leq V, \quad \forall t \in [0, T], \quad (6b)$$

$$(x(0), y(0)) = (w_{1,x}, w_{1,y}), \quad (6c)$$

$$(x(T), y(T)) = (w_{2,x}, w_{2,y}). \quad (6d)$$

Clearly, this original problem (OP) contains an infinite number of variables $(x(t), y(t))$, as there are an infinite number of time points t in the trajectory $\{x(t), y(t)\}$. Moreover, the UAV trajectory is continuous in both time and (the coordinates of the UAV's) location, which makes the trajectory design quite challenging. In addition, the objective function is apparently non-convex, which implies that an efficient optimal solution is impossible to be obtained through convex optimization technology.

To construct the optimal UAV trajectory, in the next section we introduce an equivalent mechanical problem for problem (OP) including a set of corresponding equivalent mechanical conceptions.

III. PROBLEM EQUIVALENCE IN MECHANICS

In this section, we first reformulate problem (OP), and subsequently construct a mechanical problem with exactly the same form. By introducing the concept of artificial potential energy into the trajectory design, we further show that problem (OP) can be solved by equivalently solving a mechanical problem.

A. Reformulation of Problem (OP)

Let us consider a different way of representing a UAV trajectory. Note that at each time point the UAV trajectory information can be actually fully determined if the UAV location (with moving direction) and speed are given. Hence, the whole trajectory can be described by two groups of information, namely path information and speed information. In particular, for any UAV trajectory $\{x(t), y(t)\}$, the corresponding UAV path $\{\hat{x}(s), \hat{y}(s)\}$ can be defined as

$$(\hat{x}(s), \hat{y}(s)) = (x(t), y(t)),$$

$$\text{while } \int_0^t \|\dot{x}(\tau), \dot{y}(\tau)\|_2 d\tau = s. \quad (7)$$

The path variable s denotes the path length from the given starting point D_1 to $(\hat{x}(s), \hat{y}(s))$ along the trajectory $\{x(t), y(t)\}$. Clearly, we have $s \in [0, S]$, where $S = \int_0^T \|\dot{x}(\tau), \dot{y}(\tau)\|_2 d\tau$ is the total path length of trajectory $\{x(t), y(t)\}$. Hence, the path $\{\hat{x}(s), \hat{y}(s)\}$ also starts from point D_1 and ends at point D_2 , so that $(\hat{x}(0), \hat{y}(0)) = D_1$ and $(\hat{x}(S), \hat{y}(S)) = D_2$.

On the other hand, the speed information can be expressed based on the path model. In particular, for any given path variable s , there is a unique corresponding UAV speed $v(s)$, which is given by

$$v(s) = \|\dot{x}(\tau), \dot{y}(\tau)\|_2,$$

$$\text{while } \int_0^t \|\dot{x}(\tau), \dot{y}(\tau)\|_2 d\tau = s. \quad (8)$$

Hence, (9) holds, which ensures that the UAV finishes the flight within (allocated) time duration T .

$$\int_0^S \frac{ds}{v(s)} = T \quad (9)$$

If there are hovering behaviours in the trajectory, where the UAV speed is zero, the above reformulation as well as (9) with term $\frac{1}{v(s)}$ also hold after introducing a Dirac delta function. For instance, when the UAV has a hovering behaviour at point $(\hat{x}(s_0), \hat{y}(s_0))$ with hovering duration $\Delta t > 0$, the corresponding UAV speed $v(s_0)$ becomes zero and can be expressed as

$$v(s_0) = \frac{1}{\Delta t} \cdot \frac{1}{\delta(0)}, \quad (10)$$

where $\delta(0)$ is the Dirac delta function. Note that as $\delta(0)$ is indeed infinity, the actual UAV speed $v(s_0)$ is still zero, which conforms to the hovering behaviour. However, it holds that

$$\int_{s_0-}^{s_0+} \frac{1}{v(s)} ds = \Delta t. \quad (11)$$

Following the path and speed information models, the overall throughput is then described by

$$\hat{U}(\{\hat{x}(s), \hat{y}(s)\}, v(s)) = \int_0^S R(\hat{x}(s), \hat{y}(s)) \frac{1}{v(s)} ds. \quad (12)$$

While substituting the trajectory variable $\{x(t), y(t)\}$ in problem (OP) with the variable of the path $\{\hat{x}(s), \hat{y}(s)\}$ and speed $v(s)$, problem (OP) can be equivalently reformulated as

$$(P1) : \max_{\{\hat{x}(s), \hat{y}(s)\}, v(s), S} \int_0^S R(\hat{x}(s), \hat{y}(s)) \frac{1}{v(s)} ds \quad (13a)$$

$$s.t. \frac{1}{v(s)} \geq \frac{1}{V}, \quad \forall s \in [0, S], \quad (13b)$$

$$\int_0^S \frac{1}{v(s)} ds = T, \quad (13c)$$

$$(\hat{x}(0), \hat{y}(0)) = (w_{1,x}, w_{1,y}), \quad (13d)$$

$$(\hat{x}(S), \hat{y}(S)) = (w_{2,x}, w_{2,y}). \quad (13e)$$

Note that as implied in (11), although the value of $\frac{1}{v(s)}$ may be infinite, the integral $\int_0^S \frac{1}{v(s)} ds$ is bounded by T as shown in constraint (13c). The reformulated problem (P1) requires a joint optimization of path variable $\{\hat{x}(s), \hat{y}(s)\}$, speed $v(s)$ and a total path length S , which is apparently still strenuous to be addressed via typical optimization methods.

B. Variable-Density Rope Equilibrium Problem

Now, let us consider a mechanical problem in a space with a single force field. A mass point, being with mass of M , is located at fixed position $\mathbf{D}_0 = (w_{0,x}, w_{0,y})$, i.e., the earth in Fig. 1(b). The gravitational potential generated by the mass point at any other position (\hat{x}', \hat{y}') is given by

$$R'(\hat{x}', \hat{y}') = -\frac{GM}{r(\hat{x}', \hat{y}')}, \quad (14)$$

where G is the gravitational constant, and $r(\hat{x}', \hat{y}')$ denotes the distance from point (\hat{x}', \hat{y}') to \mathbf{D}_0 as defined in (3). In addition,

a variable-density rope with mass of m is also placed in the space shown in Fig. 1(b). The two ends of the rope are fixed at positions $\mathbf{D}_1 = (w_{1,x}, w_{1,y})$ and $\mathbf{D}_2 = (w_{2,x}, w_{2,y})$, respectively. We assume that the rope is thin enough such that can be considered as a single line. We denote by a continuous functions $\{\hat{x}'(s), \hat{y}'(s)\}$ the shape of the rope, where the variable $s \in [0, S']$ represents the partial rope length from \mathbf{D}_1 to the point $(\hat{x}'(s), \hat{y}'(s))$. In addition, S' represents the total rope length, which is also a variable as the line density of the rope is changeable. Moreover, the line density $\rho(s)$ of the rope is lower-bounded by a minimum $\rho_{\min} > 0$ (which guarantees the existence of the rope, i.e., $\sqrt{(w_{1,x} - w_{2,x})^2 + (w_{1,y} - w_{2,y})^2} \cdot \rho_{\min} \leq m$). We further assume the rope to be sufficiently soft, so that each rope segment can be concentrated on a single point. For instance, with a given partial length $s_0 \in [0, S']$, if a mass point is formed at position $(\hat{x}'(s_0), \hat{y}'(s_0))$ with mass m_0 , the corresponding line density is $\rho(s_0) = m_0 \delta(0)$ with an infinite value. Although the rope density is not upper-bounded, the definite integration over it (from 0 to the given S') representing the weight of the corresponding rope segment is actually a constant, which is given by

$$\int_0^{S'} \rho(s) ds = m. \quad (15)$$

As a result, the total gravitation potential energy of the rope is then given by

$$\hat{U}'(\{\hat{x}'(s), \hat{y}'(s)\}, \rho(s)) = \int_0^{S'} R'(\hat{x}'(s), \hat{y}'(s)) \rho(s) ds. \quad (16)$$

Therefore, to study the static rope appearance, a problem minimizing the total potential energy through jointly optimizing the rope shape $\{\hat{x}'(s), \hat{y}'(s)\}$, rope density $\rho(s)$ and the total rope length S' , can be established as

$$(P2) : \min_{\{\hat{x}'(s), \hat{y}'(s)\}, \rho(s), S'} \int_0^{S'} R'(\hat{x}'(s), \hat{y}'(s)) \rho(s) ds \quad (17a)$$

$$s.t. \rho(s) \geq \rho_{\min}, \quad \forall s \in [0, S'], \quad (17b)$$

$$\int_0^{S'} \rho(s) ds = m, \quad (17c)$$

$$(\hat{x}'(0), \hat{y}'(0)) = (w_{1,x}, w_{1,y}), \quad (17d)$$

$$(\hat{x}'(S'), \hat{y}'(S')) = (w_{2,x}, w_{2,y}). \quad (17e)$$

According to the *minimum total potential energy principle* [20], if the rope has minimized the total potential energy $U'(\{\hat{x}'(s), \hat{y}'(s)\})$, i.e., being the optimal solution to (P2), it must already be in a state of equilibrium (with zero net force and zero net torque). Otherwise, with effects of nonzero net force or nonzero net torque, a better solution with lower potential energy will be found. Following the mechanical rules in equilibrium [26], we can quickly obtain the optimal solution to (P2).

C. Problem Equivalence

By carefully comparing and examining problems (P1) and (P2), we can find a set of equivalences between them, with

UAV Trajectory Design	\Rightarrow	Equivalent Mechanical Problem
UAV trajectory	\Rightarrow	density-variable rope
UAV path $\{\hat{x}(s), \hat{y}(s)\}$	\Rightarrow	rope shape $\{\hat{x}'(s), \hat{y}'(s)\}$
UAV path length S	\Rightarrow	rope length S'
UAV speed $v(s)$	\Rightarrow	reciprocal of rope line density $\frac{1}{\rho(s)}$
UAV speed limit V	\Rightarrow	reciprocal of minimum line density $\frac{1}{\rho_{\min}}$
allocated time duration T	\Rightarrow	rope mass m
maximum transmission rate $R(x, y)$	\Rightarrow	opposite of artificial potential field $-R''(x, y)$
overall throughput $\hat{U}(\{\hat{x}(s), \hat{y}(s)\}, v(s))$	\Rightarrow	opposite of artificial potential energy $-\hat{U}''(\{\hat{x}'(s), \hat{y}'(s)\}, \rho(s))$

Fig. 2. Table for problem equivalence.

which the trajectory design problem (P1) can be equivalent to a mechanical problem. More specifically, the UAV path $\{\hat{x}(s), \hat{y}(s)\}$, total path length S and UAV speed $v(s)$ can be equivalent to the rope shape $\{\hat{x}'(s), \hat{y}'(s)\}$, total rope length S' and the reciprocal of rope line density $\frac{1}{\rho(s)}$, respectively, as shown in Fig. 2. Moreover, the speed limit V and the total allocated time T equivalent respectively to the reciprocal of minimum line density $\frac{1}{\rho_{\min}}$ and the total rope mass m . Accordingly, the maximum transmission rate $R(\hat{x}(s), \hat{y}(s))$ and the overall throughput $\hat{U}(\{\hat{x}(s), \hat{y}(s)\}, v(s))$ are corresponding to the opposite of gravitational potential $-R'(\hat{x}'(s), \hat{y}'(s))$ and the opposite of total gravitation potential energy $-\hat{U}''(\{\hat{x}'(s), \hat{y}'(s)\}, \rho(s))$, respectively. On the other hand, different from these variable equivalences, the objectives of the two problems, i.e., the maximum transmission rate $R(\hat{x}(s), \hat{y}(s))$ and the gravitational potential $R'(\hat{x}'(s), \hat{y}'(s))$, have completely different expressions, as shown in (4) and (14). Thus, problems (P1) and (P2) are not equivalent, i.e., the objective of problem (P2) needs to be further reformulated.

Fortunately, as problem (P2) is constructed in a gravitational potential field $R'(x, y)$, the maximum transmission rate in (4) can be also presented via defining another artificial potential field $R''(x, y)$ in the following way: for any given position (x, y) ,

$$R''(x, y) = -R(x, y) = -B \log_2(1 + \frac{P}{\sigma^2} \frac{\beta}{r(x, y)^2 + H^2}), \quad (18)$$

which results in the same objective expression as the one of problem (P1). Hence, problem (P1) is equivalent to a variable-density rope equilibrium problem (P3) in the artificial potential field (APF) given as follows

$$(P3) : \min_{\{\hat{x}'(s), \hat{y}'(s)\}, \rho(s), S'} \hat{U}''(\{\hat{x}'(s), \hat{y}'(s)\}, \rho(s)) \quad (19a)$$

$$= \int_0^{S'} R''(\hat{x}'(s), \hat{y}'(s)) \rho(s) ds$$

s.t. (17b), (17c), (17d), (17e).

So far, the original trajectory design problem has been equivalently transformed to a mechanical problem, as described in Fig. 2. This motivates us to first rigorously solve the rope equilibrium problem (P3) in the APF (18)

by applying mechanical principles. Equivalently, the optimal trajectory for problem (OP) can be subsequently constructed from the optimal solution to problem (P3).

IV. OPTIMAL TRAJECTORY CONSTRUCTION

To optimally solve problem (P3), in this section we first characterize the properties of the defined APF and then implement mechanical principles to construct the optimal solution. In particular, different construction strategies will be presented according to different total rope masses m , i.e., equivalently different allocated time duration T in the trajectory design problem.

A. APF Characterization

As a mechanical concept, a potential field has a corresponding force field, which is a vector field and described by the negative gradient of a scalar potential function. In the considered problem (P3), the generated force field of the proposed APF $R''(x, y)$ is given by

$$\mathbf{g}(x, y) = -\nabla R''(x, y) = -\frac{dR''(x, y)}{dr(x, y)} \begin{pmatrix} \frac{\partial r(x, y)}{\partial x} \\ \frac{\partial r(x, y)}{\partial y} \end{pmatrix}. \quad (20)$$

Further note that it can be easily proved that the APF $R''(x, y)$ in (18) has a monotonic property 1.

Property 1: The APF $R''(x, y)$ in (18) is a strictly monotonically increasing function in $r(x, y)$, when $r(x, y) \geq 0$.

Hence, we have $\frac{dR''(x, y)}{dr(x, y)} > 0$ when $r(x, y) > 0$. As $r(x, y)$ denotes the distance from (x, y) to \mathbf{D}_0 , the force field $\mathbf{g}(x, y)$ is actually a vector towards a centre point \mathbf{D}_0 with an absolute value of

$$|\mathbf{g}(x, y)| = \frac{dR''(x, y)}{dr(x, y)} = \frac{2\beta BP}{\sigma^2 \ln 2} \frac{r(x, y)}{r(x, y)^2 + H^2} \frac{1}{r(x, y)^2 + H^2 + \frac{\beta P}{\sigma^2}}. \quad (21)$$

This implies that the force field $\mathbf{g}(x, y)$ is a centralized vector field with the centre at \mathbf{D}_0 . An example force field can be observed in Fig. 3(a). In addition, the force field becomes zero only when (x, y) is the same point as \mathbf{D}_0 , i.e., $r(x, y) = 0$.

Same as the general force field, when a mass point is placed in the force field, a force will act on the mass point. Similarly, when this force has done some work, the work will be equal to the reduction of the artificial potential energy on the mass point. This again indicates that for the optimal rope shape in problem (P3), which is corresponding to the optimal trajectory of problem (P1), the overall force on it cannot do any more positive work. Otherwise, a rope shape with lower artificial potential energy, namely a trajectory with higher throughput, will be found.

B. Optimal Solution With Sufficient Rope Mass

We first consider a case where the total rope mass m is sufficiently large. Due to the assumptions of density variability and minimum line density constraint on the rope, a sufficiently large m signifies that the rope has the potential to be

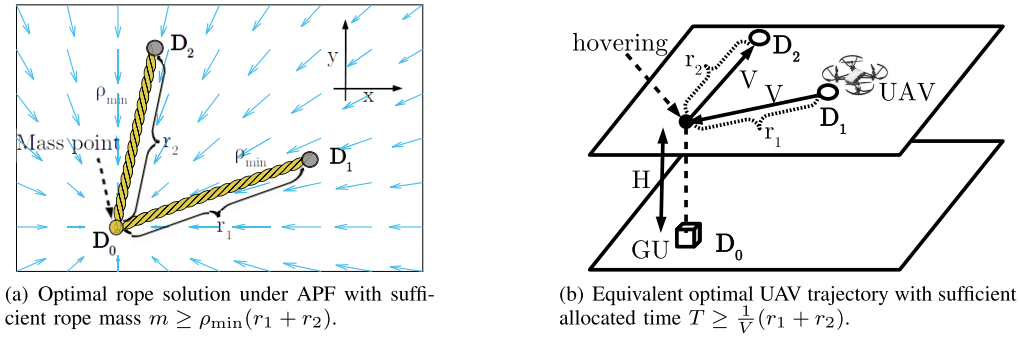


Fig. 3. Optimal solution equivalence with sufficient rope mass $m \geq \rho_{\min}(r_1 + r_2)$.

sufficiently long, since the maximum rope length is limited by $\frac{m}{\rho_{\min}}$. Furthermore, a monotonically increasing property of APF (18) has already been shown in Property 1. This indicates that a rope segment closer to point D_0 results in a lower potential energy. Thus, with sufficiently large rope mass, the optimal rope solution should approach to the centre of APF as close as possible. In other words, in the optimal rope solution, the rope traverses along straight lines with the minimum line density of ρ_{\min} from point D_1 to D_0 then to D_2 and the remaining mass forms a mass point at D_0 , as displayed in Fig. 3(a). Mathematically, the solution can be formulated as (22), (23) and (24), shown at the bottom of the page, where $r_1 = r(w_{1,x}, w_{1,y})$ and $r_2 = r(w_{2,x}, w_{2,y})$ respectively denote the distances from two ends of rope, namely D_1 and D_2 , to the center D_0 of APF. The solution is feasible only when $m \geq \rho_{\min}(r_1 + r_2)$. On the other hand, we can also mathematically prove the optimality of the constructed solution, when $m \geq \rho_{\min}(r_1 + r_2)$, as stated in Lemma 1.

Lemma 1: When $m \geq \rho_{\min}(r_1 + r_2)$, the rope defined by (22), (23) and (24) is the optimal solution of problem (P3).

Proof: The proof is provided in Appendix A. \square

Equivalently, based on the optimal solution to problem (P3) defined by (22), (23) and (24), we can further obtain the optimal trajectory of problem (OP) in the case of $T \geq \frac{1}{V}(r_1 + r_2)$. It is depicted as in Fig. 3(b) with a hovering behaviour above the GU, and can be mathematically formulated as (25), shown at the bottom of the page.

C. Optimal Solution With Insufficient Rope Mass

When $m < \rho_{\min}(r_1 + r_2)$, the maximum rope length $\frac{m}{\rho_{\min}}$ is not enough to support the rope passing the centre D_0 of APF. Hence, for any sufficiently small rope segment in the corresponding optimal rope solution, there is a non-zero force generated from APF acting on it. As a result, to minimize the total artificial potential energy, each sufficiently small rope segment in the optimal rope (solution) has extended itself towards the centre D_0 as far as possible. In other words, the optimal rope (solution) should have a constant line density ρ_{\min} , i.e., the optimal line density $\rho^*(s) = \rho_{\min}$, and accordingly an optimal total rope length $S'^* = \frac{m}{\rho_{\min}}$. Otherwise, by extending part of the rope towards D_0 , a better solution can be constructed. More rigorously, we have the statement in Lemma 2.

Lemma 2: In the optimal rope solution $\{\hat{x}^{t*}(s), \hat{y}^{t*}(s)\}$, $\rho^*(s)$ and S'^* of problem (P3), $\forall s_0 \in [0, S'^*]$, $\rho^*(s_0) = \rho_{\min}$ holds, when $(\hat{x}^{t*}(s_0), \hat{y}^{t*}(s_0)) \neq D_0 = (w_{0,x}, w_{0,y})$.

Proof: The proof is provided in Appendix B. \square

When the rope mass is insufficient, the center point D_0 will be unavailable for the rope. According to the Lemma 2, the optimal rope solution of (P3) should always have the minimum line density, i.e., $\rho^*(s) = \rho_{\min}$, with insufficient rope mass. Thus, the remaining difficulty becomes to be the design of optimal rope shape $\{\hat{x}^{t*}(s), \hat{y}^{t*}(s)\}$.

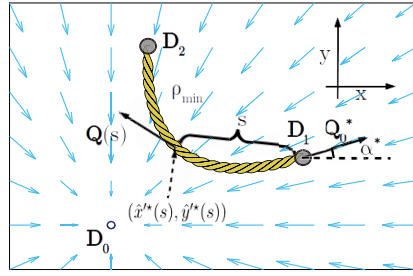
Now let us assume that in the optimal solution $\{\hat{x}^{t*}(s), \hat{y}^{t*}(s)\}$, the initial rope tension at point D_1 is given

$$S'^* = r_1 + r_2, \quad (22)$$

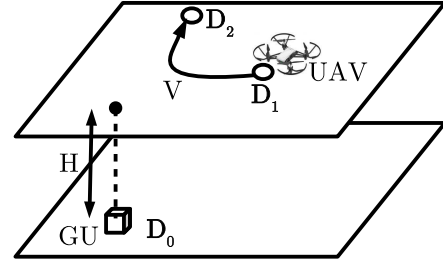
$$(\hat{x}^{t*}(s), \hat{y}^{t*}(s)) = \begin{cases} \left(\frac{s(w_{0,x} - w_{1,x})}{r_1} + w_{1,x}, \frac{s(w_{0,y} - w_{1,y})}{r_1} + w_{1,y} \right), & s \in [0, r_1], \\ \left(\frac{(s - r_1)(w_{2,x} - w_{0,x})}{r_2} + w_{0,x}, \frac{(s - r_1)(w_{2,y} - w_{0,y})}{r_2} + w_{0,y} \right), & s \in (r_1, S'^*], \end{cases} \quad (23)$$

$$\rho^*(s) = \begin{cases} (m - \rho_{\min}(r_1 + r_2))\delta(0), & s = r_1, \\ \rho_{\min}, & s \neq r_1, \end{cases} \quad (24)$$

$$(x^*(t), y^*(t)) = \begin{cases} \left(\frac{Vt(w_{0,x} - w_{1,x})}{r_1} + w_{1,x}, \frac{Vt(w_{0,y} - w_{1,y})}{r_1} + w_{1,y} \right), & t \in [0, \frac{r_1}{V}], \\ (w_{0,x}, w_{0,y}), & t \in (\frac{r_1}{V}, T - \frac{r_2}{V}], \\ \left(\frac{(Vt - T)(w_{2,x} - w_{0,x})}{r_2} + w_{2,x}, \frac{(Vt - T)(w_{2,y} - w_{0,y})}{r_2} + w_{2,y} \right), & t \in (T - \frac{r_2}{V}, T]. \end{cases} \quad (25)$$



(a) Optimal rope solution under APF with insufficient rope mass $m < \rho_{\min}(r_1 + r_2)$.



(b) Equivalent optimal UAV trajectory with insufficient allocated time $T < \frac{1}{V}(r_1 + r_2)$.

Fig. 4. Optimal solution equivalence with insufficient rope mass $m < \rho_{\min}(r_1 + r_2)$.

by \mathbf{Q}_0^* and has an angle α^* to the positive x -axis, as shown in Fig. 4(a). Then, we further denote by $\mathbf{Q}(s)$ the rope tension at point $(\hat{x}^*(s), \hat{y}^*(s))$. Note that in the optimal rope shape, the forces acting on the segment from \mathbf{D}_1 to $(\hat{x}^*(s), \hat{y}^*(s))$ must be balanced to guarantee the rope in the state of equilibrium. Thus, the net forces in the directions of x -axis and y -axis are both zero, as shown in equations (26) and (27), shown at the bottom of the page, where $A_1^*(s)$ and $A_2^*(s)$ are defined for notation simplification. Combining (26) with (27), we have

$$\frac{d\hat{y}^*(s)}{d\hat{x}^*(s)} = \frac{A_2^*(s)}{A_1^*(s)}. \quad (28)$$

Moreover, from the definition of segment length s , we have

$$\int_0^s \sqrt{1 + \left(\frac{d\hat{y}^*(s_0)}{d\hat{x}^*(s_0)}\right)^2} \frac{d\hat{x}^*(s_0)}{ds_0} ds_0 = s. \quad (29)$$

By taking derivative on both sides of (29) in s , we obtain the following relationship

$$\sqrt{\left(\frac{d\hat{x}^*(s)}{ds}\right)^2 + \left(\frac{d\hat{y}^*(s)}{ds}\right)^2} = 1. \quad (30)$$

Therefore, the first derivatives of the optimal rope shape $\{\hat{x}^*(s), \hat{y}^*(s)\}$, i.e., $\frac{d\hat{x}^*(s)}{ds}$ and $\frac{d\hat{y}^*(s)}{ds}$, can be uniquely obtained based on (26), (27), (28) and (30), which are more specifically given by

$$\frac{d\hat{x}^*(s)}{ds} = \frac{-A_1^*(s)}{\sqrt{A_1^*(s)^2 + A_2^*(s)^2}}, \quad (31)$$

$$\frac{d\hat{y}^*(s)}{ds} = \frac{-A_2^*(s)}{\sqrt{A_1^*(s)^2 + A_2^*(s)^2}}. \quad (32)$$

So far, we have found that as long as the optimal rope tension \mathbf{Q}_0^* at \mathbf{D}_1 , including $|\mathbf{Q}_0^*|$ and α^* , is known, the optimal rope solution to problem (P3) can be uniquely constructed based on (31) and (32). To sum up, with initial value

$(\hat{x}^*(0), \hat{y}^*(0)) = \mathbf{D}_1 = (w_{1,x}, w_{1,y})$, the optimal solution of (P3) with $m < \rho_{\min}(r_1 + r_2)$ is constructed as

$$(\hat{x}^*(s), \hat{y}^*(s)) = \left(\int_0^s \frac{-A_1^*(s)ds}{\sqrt{A_1^*(s)^2 + A_2^*(s)^2}} + w_{1,x}, \int_0^s \frac{-A_2^*(s)ds}{\sqrt{A_1^*(s)^2 + A_2^*(s)^2}} + w_{1,y} \right), \quad (33)$$

$$\rho^*(s) = \rho_{\min}, \quad \forall s \in [0, S^* \triangleq \frac{m}{\rho_{\min}}]. \quad (34)$$

Equivalently, the optimal UAV trajectory $\{x^*(t), y^*(t)\}$ for original problem (OP) in case of $T < \frac{r_1 + r_2}{V}$ can be constructed, as shown in Fig. 4(b). It is given by

$$(x^*(t), y^*(t)) = (\hat{x}^*(Vt), \hat{y}^*(Vt)), \quad (35)$$

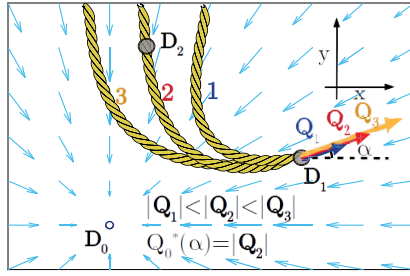
where $V = 1/\rho_{\min}$.

V. OPTIMAL INITIAL ROPE TENSION DESIGN

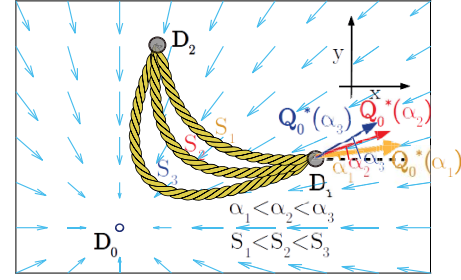
So far, the optimal solution of UAV trajectory has been constructed. However, from the above results, we learn that to obtain the optimal solution with insufficient rope mass $m < \rho_{\min}(r_1 + r_2)$, it is essential to design the optimal rope tension \mathbf{Q}_0^* at \mathbf{D}_1 . Actually, the optimal rope tension can be quickly obtained by simply greedily searching the optimal values of two parameters, i.e., the absolute value Q_0 and the tension angle α . More specifically, with a fixed angle α of initial tension at \mathbf{D}_1 , a larger absolute value Q_0 makes the constructed rope always closer to the centre \mathbf{D}_0 , as implied in Fig. 5(a). Therefore, for any given angle α , there exists a unique absolute value $Q_0^*(\alpha)$ making the rope exactly pass the destination \mathbf{D}_2 . More importantly, this value $Q_0^*(\alpha)$ can be simply found by fixing α and greedily searching over the absolute value Q_0 . On the other hand, with $Q_0 = Q_0^*(\alpha)$, the rope length between \mathbf{D}_1 and \mathbf{D}_2 is actually monotonically increasing with respect to the angle α , as shown in Fig. 5(b). Hence, with given $Q_0 = Q_0^*(\alpha)$, the optimal initial tension

$$|\mathbf{Q}_0^*| \cos \alpha^* + \underbrace{\int_0^s |\mathbf{g}(\hat{x}^*(s_0), \hat{y}^*(s_0))| \rho_{\min} \frac{w_{0,x} - \hat{x}^*(s_0)}{r(\hat{x}^*(s_0), \hat{y}^*(s_0))} ds_0}_{A_1^*(s)} + |\mathbf{Q}(s)| \frac{d\hat{x}^*(s)}{ds} = 0, \quad (26)$$

$$|\mathbf{Q}_0^*| \sin \alpha^* + \underbrace{\int_0^s |\mathbf{g}(\hat{x}^*(s_0), \hat{y}^*(s_0))| \rho_{\min} \frac{w_{0,y} - \hat{y}^*(s_0)}{r(\hat{x}^*(s_0), \hat{y}^*(s_0))} ds_0}_{A_2^*(s)} + |\mathbf{Q}(s)| \frac{d\hat{y}^*(s)}{ds} = 0. \quad (27)$$

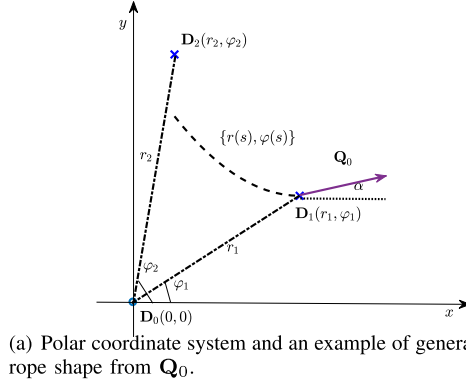


(a) Constructed ropes with different absolute values of initial tension at D_1 .

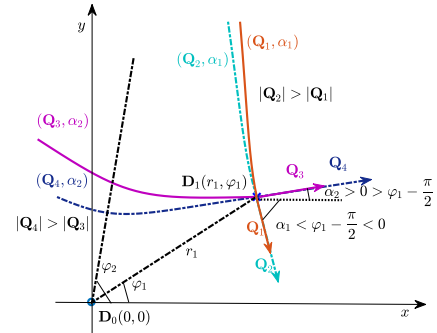


(b) Constructed ropes with different initial tension angles and already optimized absolute value.

Fig. 5. Monotonic effects of initial rope tension at D_1 on the constructed ropes.



(a) Polar coordinate system and an example of generated rope shape from Q_0 .



(b) Effect of Q_0 on the generated rope shape with different given α .

Fig. 6. Polar coordinate system and the monotonic effect of rope tension.

Q_0^* can be uniquely found by further greedily searching over angle α .

In this section, we provide rigorous proofs for the above stated monotonic impacts of absolute value Q_0 and tension angle α , in purpose of guaranteeing the global optimality of our design. To start with, we first derive a closed-form rope shape expression in the polar coordinate system, based on which the effect analysis for initial rope tension can be significantly facilitated. Then, the impact of the initial rope tension on constructed rope will be addressed subsequently.

A. Closed-Form Expression in Polar Coordinate System

We first consider a polar coordinate system (r, φ) with original point defined as the center D_0 of APF, as shown in Fig. 6(a). In the polar coordinate system, the coordinates of two rope endpoints, namely points D_1 and D_2 with Cartesian coordinates $(w_{1,x}, w_{1,y})$ and $(w_{2,x}, w_{2,y})$, are respectively given by (r_1, φ_1) and (r_2, φ_2) . Without loss of generality, we assume $\varphi_2 > \varphi_1$. In addition, the rope shape $\{\hat{x}'(s), \hat{y}'(s)\}$ is transformed to $\{r(s), \varphi(s)\}$, according to the following relations

$$\hat{x}'(s) = r(s) \cos \varphi(s), \quad \hat{y}'(s) = r(s) \sin \varphi(s). \quad (36)$$

Note that with any initial rope tension Q_0 at D_1 , i.e., including an absolute value $Q_0 = |Q_0|$ and angle α , the rope shape $\{\hat{x}'(s), \hat{y}'(s)\}$ can be uniquely determined by replacing $|Q_0^*|$ and α^* respectively with $|Q_0|$ and α given in (26) and (27). An example generated rope shape $(r(s), \varphi(s))$ is shown in Fig. 6(a). It should be mentioned that with a random initial

rope tension Q_0 , the generated rope shape does not necessarily pass through the other endpoint D_2 .

Note that the optimal rope shape $\{\hat{x}'^*(s), \hat{y}'^*(s)\}$ is strictly limited in the triangle area formed by D_i , $i \in \{0, 1, 2\}$. Accordingly, the angle α^* of optimal tension Q_0^* is bounded in interval $[\arctan \frac{w_{2,y} - w_{1,y}}{w_{2,x} - w_{1,x}}, \varphi_1]$. Therefore, we assume $\alpha \in [\arctan \frac{w_{2,y} - w_{1,y}}{w_{2,x} - w_{1,x}}, \varphi_1]$.

In the polar coordinate system, for any given initial rope tension Q_0 at D_1 , we have the following relation for the generated rope shape $\{r(s), \varphi(s)\}$,

$$\begin{aligned} \frac{A_2(s)}{A_1(s)} &= \frac{d\hat{x}'(s)}{d\hat{y}'(s)} = \frac{d(r(s) \cos \varphi(s))}{d(r(s) \sin \varphi(s))} \\ &= \frac{r(s) \frac{d\varphi(s)}{dr(s)} + \tan \varphi(s)}{1 - r(s) \frac{d\varphi(s)}{dr(s)} \tan \varphi(s)}, \end{aligned} \quad (37)$$

where $A_1(s)$ and $A_2(s)$ are modified equations (26) and (27) by replacing $|Q_0^*|$ and α^* respectively with $|Q_0|$ and α . The expressions of $A_1(s)$ and $A_2(s)$ in the polar coordinate system are given by

$$A_1(s) = Q_0 \cos \alpha + \int_0^s g(r(s_0)) \rho_{\min}(-\cos \varphi(s_0)) ds_0, \quad (38)$$

$$A_2(s) = Q_0 \sin \alpha + \int_0^s g(r(s_0)) \rho_{\min}(-\sin \varphi(s_0)) ds_0, \quad (39)$$

where $g(r(s))$ is defined as the absolute value of fore field with distance to center point $r(s)$, i.e., $g(r(s)) = |g(x, y)|$, when $\sqrt{x^2 + y^2} = r(s)$. And from the equation (37), we can

also obtain that

$$r(s) \frac{d\varphi(s)}{dr(s)} = \frac{\frac{A_2(s)}{A_1(s)} - \tan \varphi(s)}{1 + \frac{A_2(s)}{A_1(s)} \tan \varphi(s)}. \quad (40)$$

In the following, in order to gain a deep insight of the relation between $r(s)$ and $\varphi(s)$ with given \mathbf{Q}_0 , we make efforts to construct an equation containing only variables $r(s)$ and $\varphi(s)$. To facilitate the formulation of generated rope shape in the polar coordinate system, we first introduce a Lemma 3 regarding the relation between $A_1(s)$ and $A_2(s)$ with a given \mathbf{Q}_0 .

Lemma 3: For a given \mathbf{Q}_0 , in the generated $\{r(s), \varphi(s)\}$ from (40), the value of $A_1(s)r(s) \sin \varphi(s) - A_2(s)r(s) \cos \varphi(s)$ is constant in s . Namely,

$$A_1(s)r(s) \sin \varphi(s) - A_2(s)r(s) \cos \varphi(s) = r_1 Q_0 \sin(\varphi_1 - \alpha) \triangleq \hat{Q}_0. \quad (41)$$

Proof: We prove the lemma by studying the first-order derivative of the term $A_1(s)r(s) \sin \varphi(s) - A_2(s)r(s) \cos \varphi(s)$ in s , which is obtained as

$$\begin{aligned} & \frac{dA_1(s)r(s) \sin \varphi(s) - A_2(s)r(s) \cos \varphi(s)}{ds} \\ &= g(r(s))\rho_{\min}(-\cos \varphi(s))r(s) \sin \varphi(s) \\ & \quad - g(r(s))\rho_{\min}(-\sin \varphi(s))r(s) \cos \varphi(s) \\ & \quad + (A_1(s) \sin \varphi(s) - A_2(s) \cos \varphi(s)) \frac{dr(s)}{ds} \\ & \quad + (A_1(s) \cos \varphi(s) + A_2(s) \sin \varphi(s))r(s) \frac{d\varphi(s)}{ds}. \end{aligned} \quad (42)$$

Considering the relation (40) between $\frac{dr(s)}{ds}$ and $\frac{d\varphi(s)}{ds}$, the above derivative becomes zero, and the constant value of $A_1(s)r(s) \sin \varphi(s) - A_2(s)r(s) \cos \varphi(s)$ can be derived to be equal to its initial value $A_1(0)r(0) \sin \varphi(0) - A_2(0)r(0) \cos \varphi(0) = r_1 Q_0 \sin(\varphi_1 - \alpha) \triangleq \hat{Q}_0$. \square

Remark 1: Note that Lemma 3 substantially represents the zero net torque requirement in the equilibrium state. The torque is taken with respect to the origin point and the value \hat{Q}_0 is actually the resulted torque by \mathbf{Q}_0 with respect to the origin \mathbf{D}_0 . As the force field in APF is always towards origin \mathbf{D}_0 , the torque resulted from $\mathbf{Q}(s)$, namely $A_1(s)r(s) \sin \varphi(s) - A_2(s)r(s) \cos \varphi(s)$, remains to be a constant.

Combining (37) and (41), we find that $A_1(s)$ and $A_2(s)$ can be completely represented by $r(s)$, $\varphi(s)$ and $\frac{d\varphi(s)}{dr(s)}$, namely

$$A_1(s) = -\frac{\hat{Q}_0 \left(1 - r(s) \frac{d\varphi(s)}{dr(s)} \tan \varphi(s)\right)}{r(s)^2 \frac{d\varphi(s)}{dr(s)} \frac{1}{\cos \varphi(s)}}, \quad (43)$$

$$A_2(s) = -\frac{\hat{Q}_0 \left(r(s) \frac{d\varphi(s)}{dr(s)} + \tan \varphi(s)\right)}{r(s)^2 \frac{d\varphi(s)}{dr(s)} \frac{1}{\cos \varphi(s)}}. \quad (44)$$

Then, by taking derivative of both sides of (40) to s , we can correspondingly get an expression of $\frac{d(r(s) \frac{d\varphi(s)}{dr(s)})}{ds}$ which contains the function term of $A_1(s)$ and $A_2(s)$. However, according to (43) and (44), the expression of $\frac{d(r(s) \frac{d\varphi(s)}{dr(s)})}{ds}$ can be

simplified after a series of reformulation. Finally, we have

$$\begin{aligned} \frac{d\left(r(s) \frac{d\varphi(s)}{dr(s)}\right)}{ds} &= -\frac{d\varphi(s)}{ds} \left(\left(r(s) \frac{d\varphi(s)}{dr(s)}\right)^2 + 1 \right) \\ & \quad - \left(r(s) \frac{d\varphi(s)}{dr(s)}\right)^2 \frac{g(r(s))\rho_{\min}r(s)}{\hat{Q}_0}, \end{aligned} \quad (45)$$

which does not contain any terms of $A_1(s)$ and $A_2(s)$. In the same way, we obtain that

$$\begin{aligned} \frac{dr(s)}{ds} &= \frac{-A_1(s) \cos \varphi(s) - A_2(s) \sin \varphi(s)}{\sqrt{A_1(s)^2 + A_2(s)^2}} \\ &= \frac{\text{sgn}\left(\frac{dr(s)}{ds}\right)}{\sqrt{\left(r(s) \frac{d\varphi(s)}{dr(s)}\right)^2 + 1}}, \end{aligned} \quad (46)$$

where $\text{sgn}\left(\frac{dr(s)}{ds}\right)$ indicates the sign of $\frac{dr(s)}{ds}$. Thus, by combining the above two equations, we have

$$\begin{aligned} \frac{d\left(r(s) \frac{d\varphi(s)}{dr(s)}\right)}{dr(s)} &= -\frac{d\varphi(s)}{dr(s)} \left(\left(r(s) \frac{d\varphi(s)}{dr(s)}\right)^2 + 1 \right) \\ & \quad - \text{sgn}\left(\frac{dr(s)}{ds}\right) \left(r(s) \frac{d\varphi(s)}{dr(s)}\right)^2 \\ & \quad \sqrt{\left(r(s) \frac{d\varphi(s)}{dr(s)}\right)^2 + 1} \frac{g(r(s))\rho_{\min}r(s)}{\hat{Q}_0}. \end{aligned} \quad (47)$$

Note that besides $r(s)$ and $\varphi(s)$, the only remaining variable in the above equation is the variable s in the discontinuous function $\text{sgn}\left(\frac{dr(s)}{ds}\right)$. To further simplify the equation, we first discuss the sign of $\frac{d\varphi(s)}{ds}$. Following the same process of obtaining $\frac{dr(s)}{ds}$, $\frac{d\varphi(s)}{ds}$ is given by

$$\begin{aligned} \frac{d\varphi(s)}{ds} &= \frac{A_1(s)r(s) \sin \varphi(s) - A_2(s)r(s) \cos \varphi(s)}{r(s)^2 \sqrt{A_1(s)^2 + A_2(s)^2}} \\ &= \frac{r_1 Q_0 \sin(\varphi_1 - \alpha)}{r(s)^2 \sqrt{A_1(s)^2 + A_2(s)^2}}. \end{aligned} \quad (48)$$

It is already assumed that the angle α is limited in interval $\alpha \in [\arctan \frac{w_{2,y}-w_{1,y}}{w_{2,x}-w_{1,x}}, \varphi_1]$ and we have $\arctan \frac{w_{2,y}-w_{1,y}}{w_{2,x}-w_{1,x}} > \varphi_1 - \pi$ to make sure $\varphi_2 > \varphi_1$. Thus, we always have $\frac{d\varphi(s)}{ds} > 0$, $\frac{d(r(s) \frac{d\varphi(s)}{dr(s)})}{ds} < 0$ and correspondingly, $\text{sgn}\left(\frac{dr(s)}{ds}\right) = \text{sgn}\left(\frac{dr(s)}{d\varphi(s)}\right) \text{sgn}\left(\frac{d\varphi(s)}{ds}\right) = \text{sgn}\left(\frac{dr(s)}{d\varphi(s)}\right)$. Subsequently, the equation (47) can be reformulated as a form with only variables $r(s)$ and $\varphi(s)$ involved, namely

$$\begin{aligned} & \frac{d\left(\sqrt{\left(\frac{1}{r(s)} \frac{dr(s)}{d\varphi(s)}\right)^2 + 1}\right)}{dr(s)} \\ &= \frac{1}{r(s)} \sqrt{\left(\frac{1}{r(s)} \frac{dr(s)}{d\varphi(s)}\right)^2 + 1} + \frac{g(r(s))\rho_{\min}r(s)}{\hat{Q}_0}. \end{aligned} \quad (49)$$

We observe that the equation (49) is actually a linear differential equation of $\sqrt{\left(\frac{1}{r(s)} \frac{dr(s)}{d\varphi(s)}\right)^2 + 1}$ with respect to $r(s)$. According to [27], we can build the solution for equation

(49) as

$$\begin{aligned} & \sqrt{\left(\frac{1}{r(s)} \frac{dr(s)}{d\varphi(s)}\right)^2 + 1} \\ &= \frac{\rho_{\min}}{\hat{Q}_0} r(s) \int_{r_1}^{r(s)} g(r_0) dr_0 + \frac{r(s)}{r_1} \frac{1}{\sin(\varphi_1 - \alpha)}, \quad (50) \end{aligned}$$

where the initial value is $\sqrt{\left(\frac{1}{r(s)} \frac{dr(s)}{d\varphi(s)}\right)^2 + 1} \Big|_{s=0} = \frac{1}{\sin(\varphi_1 - \alpha)}$. And a more visualized result for $\frac{dr(s)}{d\varphi(s)}$ is

$$\left| \frac{dr(s)}{d\varphi(s)} \right| = r(s) \sqrt{\left(\frac{\rho_{\min}}{\hat{Q}_0} r(s) \int_{r_1}^{r(s)} g(r_0) dr_0 + \frac{r(s)}{r_1} \frac{1}{\sin(\varphi_1 - \alpha)} \right)^2 - 1}. \quad (51)$$

Moreover, with the conclusions $\frac{d\varphi(s)}{ds} > 0$ and $\frac{d(r(s) \frac{d\varphi(s)}{dr(s)})}{ds} < 0$, we obtain that

$$\frac{d\left(\frac{dr(s)}{d\varphi(s)}\right)}{d\varphi(s)} = \frac{1}{\frac{d\varphi(s)}{ds}} \left(\frac{d\varphi(s)}{ds} - \frac{d\left(r(s) \frac{d\varphi(s)}{dr(s)}\right)}{ds} \right) \frac{1}{r(s) \left(\frac{d\varphi(s)}{dr(s)}\right)^2} > 0, \quad (52)$$

so that $r(s)$ is proved to be convex in $\varphi(s)$. Then based on (51), we can directly focus on the variation tendency of $r(s)$ to $\varphi(s)$. Note that different initial value and sign of $\frac{dr(s)}{d\varphi(s)}$ at $s = 0$ will lead to different variation tendency of $r(s)$. Therefore, we next formulate the closed-form expression of $\varphi(s)$ in $r(s)$, respectively under two cases regarding the initial sign of $\frac{dr(s)}{d\varphi(s)}$.

- When $\frac{dr(s)}{d\varphi(s)} \Big|_{s=0} \geq 0$, as $r(s)$ is convex in $\varphi(s)$, we have $\forall s \geq 0$, $\frac{dr(s)}{d\varphi(s)} \geq 0$ holds and both $\frac{dr(s)}{d\varphi(s)}$ and $r(s)$ are continuously increasing with respect to $\varphi(s)$. As a result, we have the closed-form expression (53), which is shown at the bottom of the page.
- When $\frac{dr(s)}{d\varphi(s)} \Big|_{s=0} < 0$, as $r(s)$ is convex in $\varphi(s)$, $\frac{dr(s)}{d\varphi(s)}$ is also continuously increasing in $\varphi(s)$. Therefore, with $\varphi(s)$ increasing, $r(s)$ will continuously decrease to a minimum r_{\min} where $\frac{dr(s)}{d\varphi(s)} \Big|_{r=r_{\min}} = 0$, and then continuously increase from the minimum. According to (51), the term $\frac{\rho_{\min}}{\hat{Q}_0} r(s) \int_{r_1}^{r(s)} g(r_0) dr_0 + \frac{r(s)}{r_1} \frac{1}{\sin(\varphi_1 - \alpha)}$ has a positive initial value $\frac{1}{\sin(\varphi_1 - \alpha)}$ and is decreasing in $r(s)$.

Thus, the minimum r_{\min} can be uniquely obtained by solving the following equation

$$\frac{\rho_{\min}}{\hat{Q}_0} r_{\min} \int_{r_1}^{r_{\min}} g(r_0) dr_0 + \frac{r_{\min}}{r_1} \frac{1}{\sin(\varphi_1 - \alpha)} = 1. \quad (54)$$

To sum up, the relation between $\varphi(s)$ and $r(s)$ can be described as (55), shown at the bottom of the page, where $H(\hat{Q}_0, \alpha)$ denotes difference of $\varphi(s)$ when s varies from $s = 0$ to $s = s_0$ when $r(s_0) = r_{\min}$, i.e., $H(\hat{Q}_0, \alpha) = \int_{r_1}^{r_{\min}} \frac{-dr_0}{r_0 \sqrt{\left(\frac{\rho_{\min}}{\hat{Q}_0} r_0 \int_{r_1}^{r_0} g(r'_0) dr'_0 + \frac{r_0}{r_1} \frac{1}{\sin(\varphi_1 - \alpha)}\right)^2 - 1}}$.

Note that the relations (53) and (55) between $r(s)$ and $\varphi(s)$ hold in the generated rope shape only when $\alpha \in (\varphi_1 - \pi, \varphi_1)$, which makes $\sin(\varphi_1 - \alpha) > 0$, namely $\frac{d\varphi(s)}{ds} > 0$ according to (48). More specifically, when $\alpha \in [\varphi_1 - \frac{\pi}{2}, \varphi_1)$, the relation between $r(s)$ and $\varphi(s)$ is represented by (53), while (55) holds when $\alpha \in (\varphi_1 - \pi, \varphi_1 - \frac{\pi}{2})$.

B. Effect Analysis for Initial Rope Tension

Based on the above characterizations/discussions in the polar coordinate system, in the following we study the effect of tension value Q_0 on the generated rope shape, as illustrated in Lemma 4.

Lemma 4: With a fixed tension angle $\alpha \in (\varphi_1 - \pi, \varphi_1)$, in the generated rope shape $\{r(s), \varphi(s)\}$, $\forall \varphi_0 > \varphi_1$, the corresponding $r(s)$ when $\varphi(s) = \varphi_0$ is monotonically decreasing with respect to tension value Q_0 .

Proof: As indicated by (41), with given α , \hat{Q}_0 is positively proportional to Q_0 . For facilitation, we study the effect of \hat{Q}_0 instead, and the same conclusion will be proved. From the previous discussions, we have different closed-form relations between $r(s)$ and $\varphi(s)$, i.e., equations (53) and (55), corresponding to different initial value of $\frac{dr(s)}{d\varphi(s)}$. Hence, the effect of \hat{Q}_0 should also be investigated in two different cases.

Case I: $\frac{dr(s)}{d\varphi(s)} \Big|_{s=0} \geq 0$. $\forall \varphi_0 > \varphi_1$, when $\varphi(s) = \varphi_0$, we have $r(s) > r_1$ and

$$\int_{r_1}^{r(s)} \frac{dr_0}{r_0 \sqrt{\left(\frac{\rho_{\min}}{\hat{Q}_0} r_0 \int_{r_1}^{r_0} g(r'_0) dr'_0 + \frac{r_0}{r_1} \frac{1}{\sin(\varphi_1 - \alpha)}\right)^2 - 1}} = \varphi_0 - \varphi_1. \quad (56)$$

As the right side of the above equation is a constant, by taking differentiation, we can obtain the relation between $r(s)$ and

$$\varphi(s) - \varphi_1 = \int_{r_1}^{r(s)} \frac{dr_0}{r_0 \sqrt{\left(\frac{\rho_{\min}}{\hat{Q}_0} r_0 \int_{r_1}^{r_0} g(r'_0) dr'_0 + \frac{r_0}{r_1} \frac{1}{\sin(\varphi_1 - \alpha)}\right)^2 - 1}}. \quad (53)$$

$$\varphi(s) - \varphi_1 = \begin{cases} \int_{r_1}^{r(s)} \frac{-dr_0}{r_0 \sqrt{\left(\frac{\rho_{\min}}{\hat{Q}_0} r_0 \int_{r_1}^{r_0} g(r'_0) dr'_0 + \frac{r_0}{r_1} \frac{1}{\sin(\varphi_1 - \alpha)}\right)^2 - 1}}, & \text{when } \frac{dr(s)}{d\varphi(s)} \leq 0, \\ 2H(\hat{Q}_0, \alpha) + \int_{r_1}^{r(s)} \frac{dr_0}{r_0 \sqrt{\left(\frac{\rho_{\min}}{\hat{Q}_0} r_0 \int_{r_1}^{r_0} g(r'_0) dr'_0 + \frac{r_0}{r_1} \frac{1}{\sin(\varphi_1 - \alpha)}\right)^2 - 1}}, & \text{when } \frac{dr(s)}{d\varphi(s)} > 0, \end{cases} \quad (55)$$

\hat{Q}_0 :

$$\frac{dr(s)}{d\hat{Q}_0} = - \frac{H_0(\hat{Q}_0, \alpha, r_1, r(s))}{r(s) \sqrt{\left(\frac{\rho_{\min}}{\hat{Q}_0} r(s) \int_{r_1}^{r(s)} g(r'_0) dr'_0 + \frac{r(s)}{r_1} \frac{1}{\sin(\varphi_1 - \alpha)} \right)^2 - 1}}. \quad (57)$$

where the expression $H_0(\hat{Q}_0, \alpha, r', r'')$ is defined as (58), shown at the bottom of the page for simplification. Therefore, as $r(s) > r_1$ and $r_0 \in [r_1, r(s)]$, we have $H_0(\hat{Q}_0, \alpha, r_1, r(s)) > 0$ and $\frac{dr(s)}{d\hat{Q}_0} < 0$ for $\varphi(s) = \varphi_0$. A larger \hat{Q}_0 , i.e., larger Q_0 , results in a smaller $r(s)$ for a given $\varphi(s)$.

Case II: $\frac{dr(s)}{d\varphi(s)} \Big|_{s=0} < 0$. If $\varphi_0 > \varphi_1$ makes $\frac{dr(s)}{d\varphi(s)} \Big|_{\varphi(s)=\varphi_0} \leq 0$, according to (55), when $\varphi(s) = \varphi_0$, $\frac{dr(s)}{d\hat{Q}_0}$ can be obtained to be the same form as (57). Differently, we have $r(s) < r_1$ and $r_0 \in [r(s), r_1]$, which still result in $H_0(\hat{Q}_0, \alpha, r_1, r(s)) > 0$ and $\frac{dr(s)}{d\hat{Q}_0} < 0$ for $\varphi(s) = \varphi_0$.

If $\varphi_0 > \varphi_1$ makes $\frac{dr(s)}{d\varphi(s)} \Big|_{\varphi(s)=\varphi_0} > 0$, according to (55), when $\varphi(s) = \varphi_0$, $\frac{dr(s)}{d\hat{Q}_0}$ is given by

$$\frac{dr(s)}{d\hat{Q}_0} = - \frac{2 \frac{dH(\hat{Q}_0, \alpha)}{d\hat{Q}_0} + H_0(\hat{Q}_0, \alpha, r_1, r(s))}{r(s) \sqrt{\left(\frac{\rho_{\min}}{\hat{Q}_0} r(s) \int_{r_1}^{r(s)} g(r'_0) dr'_0 + \frac{r(s)}{r_1} \frac{1}{\sin(\varphi_1 - \alpha)} \right)^2 - 1}}. \quad (59)$$

Obviously, based on previous discussions, if $\frac{dH(\hat{Q}_0, \alpha)}{d\hat{Q}_0} \geq 0$ for given α , we will get a conclusion of $\frac{dr(s)}{d\hat{Q}_0} < 0$ for $\varphi(s) = \varphi_0$, $\forall \varphi_0 > 0$ for all cases. And $r(s)$ when $\varphi(s) = \varphi_0$ can be proved to be monotonically decreasing with respect to \hat{Q}_0 , i.e., monotonically decreasing with respect to Q_0 .

Finally, we prove that $\frac{dH(\hat{Q}_0, \alpha)}{d\hat{Q}_0} \geq 0$ holds for given α to finalize the proof. At first, r_{\min} is dependent in \hat{Q}_0 according to (54), and the derivative is formulated as

$$\frac{dr_{\min}}{d\hat{Q}_0} = \frac{\frac{\rho_{\min}}{\hat{Q}_0^2} r_{\min} \int_{r_1}^{r_{\min}} g(r_0) dr_0}{\frac{1}{r_{\min}} + \frac{\rho_{\min}}{\hat{Q}_0} r_{\min} g(r_{\min})} < 0, \text{ as } r_{\min} < r_1. \quad (60)$$

Then, the derivative of function $H(\hat{Q}_0, \alpha)$ over \hat{Q}_0 is formulated as

$$\begin{aligned} \frac{dH(\hat{Q}_0, \alpha)}{d\hat{Q}_0} &= -H_0(\hat{Q}_0, \alpha, r_1, r_{\min}) \\ &\quad + \frac{-\frac{dr_{\min}}{d\hat{Q}_0}}{r_{\min} \sqrt{\left(\frac{\rho_{\min}}{\hat{Q}_0} r_{\min} \int_{r_1}^{r_{\min}} g(r_0) dr_0 + \frac{r_{\min}}{r_1} \frac{1}{\sin(\varphi_1 - \alpha)} \right)^2 - 1}}. \end{aligned} \quad (61)$$

Taking the relation between r_{\min} and \hat{Q}_0 (54) into account, $\frac{dH(\hat{Q}_0, \alpha)}{d\hat{Q}_0}$ is indeed the difference between two positive infinite values. However, we can still get the sign of $\frac{dH(\hat{Q}_0, \alpha)}{d\hat{Q}_0}$ via some tricks. By introducing a variable z

$$z(r_0) = \left(\frac{\rho_{\min}}{\hat{Q}_0} r_0 \int_{r_1}^{r_0} g(r'_0) dr'_0 + \frac{r_0}{r_1} \frac{1}{\sin(\varphi_1 - \alpha)} \right)^2 - 1, \quad (62)$$

and a sufficiently small value ϵ for representing the term $\left(\frac{\rho_{\min}}{\hat{Q}_0} r_{\min} \int_{r_1}^{r_{\min}} g(r_0) dr_0 + \frac{r_{\min}}{r_1} \frac{1}{\sin(\varphi_1 - \alpha)} \right)^2 - 1$, we have the reformulated $\frac{dH(\hat{Q}_0, \alpha)}{d\hat{Q}_0}$ as (63), shown at the bottom of the page, where r_0 is also a function of z and $z(r_{\min}) = 0$. Next, we compare it with ϵ^{-1} , namely as shown in (64) at the bottom of the page. As $\lim_{\epsilon \rightarrow 0+} \frac{1}{\epsilon} = +\infty$, it is eventually proved that $\frac{dH(\hat{Q}_0, \alpha)}{d\hat{Q}_0} \geq 0$ holds for a fixed angle α .

To more intuitively show the effects of initial tension value Q_0 with given α , examples for both Case I and Case II are displayed in Fig. 6(b). For Case I, two rope shapes are generated by \mathbf{Q}_1 and \mathbf{Q}_2 ($|\mathbf{Q}_2| > |\mathbf{Q}_1|$) with $\alpha = \alpha_1$. And the examples of the generated rope shapes by \mathbf{Q}_3 and \mathbf{Q}_4 ($|\mathbf{Q}_4| > |\mathbf{Q}_3|$) with $\alpha = \alpha_2$ belong to Case II. \square

According to Lemma 4, for given α , a larger value of Q_0 always results in a generated rope closer to \mathbf{D}_0 . Thus, through greedily searching of Q_0 , the unique corresponding

$$H_0(\hat{Q}_0, \alpha, r', r'') = \int_{r'}^{r''} \frac{\left(\frac{\rho_{\min}}{\hat{Q}_0} r_0 \int_{r_1}^{r_0} g(r'_0) dr'_0 + \frac{r_0}{r_1} \frac{1}{\sin(\varphi_1 - \alpha)} \right) \left(\frac{\rho_{\min}}{\hat{Q}_0^2} r_0 \int_{r_1}^{r_0} g(r'_0) dr'_0 \right)}{r_0 \left(\sqrt{\left(\frac{\rho_{\min}}{\hat{Q}_0} r_0 \int_{r_1}^{r_0} g(r'_0) dr'_0 + \frac{r_0}{r_1} \frac{1}{\sin(\varphi_1 - \alpha)} \right)^2 - 1}} \right)^3} dr_0 \quad (58)$$

$$\frac{dH(\hat{Q}_0, \alpha)}{d\hat{Q}_0} = \lim_{\epsilon \rightarrow 0+} \left(\frac{-1}{r_{\min} \sqrt{\epsilon}} \frac{dr_{\min}}{d\hat{Q}_0} - \int_{z(r_1)}^{\epsilon} \frac{\frac{1}{2r_0} \frac{\rho_{\min}}{\hat{Q}_0^2} r_0 \int_{r_1}^{r_0} g(r'_0) dr'_0}{\frac{\rho_{\min}}{\hat{Q}_0} \int_{r_1}^{r_0} g(r'_0) dr'_0 + \frac{1}{r_1} \frac{1}{\sin(\varphi_1 - \alpha)} + \frac{\rho_{\min}}{\hat{Q}_0} r_0 g(r_0)} z^{-\frac{3}{2}} dz \right), \quad (63)$$

$$\begin{aligned} &\lim_{\epsilon \rightarrow 0+} \frac{\frac{-1}{r_{\min} \sqrt{\epsilon}} \frac{dr_{\min}}{d\hat{Q}_0} - \int_{z(r_1)}^{\epsilon} \frac{\frac{1}{2r_0} \frac{\rho_{\min}}{\hat{Q}_0^2} r_0 \int_{r_1}^{r_0} g(r'_0) dr'_0}{\frac{\rho_{\min}}{\hat{Q}_0} \int_{r_1}^{r_0} g(r'_0) dr'_0 + \frac{1}{r_1} \frac{1}{\sin(\varphi_1 - \alpha)} + \frac{\rho_{\min}}{\hat{Q}_0} r_0 g(r_0)} z^{-\frac{3}{2}} dz}{\epsilon^{-1}} \\ &= \lim_{\epsilon \rightarrow 0+} \left(\frac{-\sqrt{\epsilon} \frac{dr_{\min}}{d\hat{Q}_0}}{r_{\min}} + \frac{\frac{\sqrt{\epsilon}}{2r_{\min}} \frac{\rho_{\min}}{\hat{Q}_0^2} r_{\min} \int_{r_1}^{r_{\min}} g(r'_0) dr'_0}{\frac{\rho_{\min}}{\hat{Q}_0} \int_{r_1}^{r_{\min}} g(r'_0) dr'_0 + \frac{1}{r_1} \frac{1}{\sin(\varphi_1 - \alpha)} + \frac{\rho_{\min}}{\hat{Q}_0} r_{\min} g(r_{\min})} \right) \\ &= \lim_{\epsilon \rightarrow 0+} \frac{-\sqrt{\epsilon} \frac{dr_{\min}}{d\hat{Q}_0}}{2r_{\min}} = 0+, \text{ as } \frac{dr_{\min}}{d\hat{Q}_0} < 0. \end{aligned} \quad (64)$$

$Q_0 = Q_0^*(\alpha)$ can be found, with which the generated rope $\{r(s), \varphi(s)\}$ passes through the destination $\mathbf{D}_2(r_2, \varphi_2)$.

C. Effect of α on Generated Rope Shape

On the other hand, the angle α for initial rope tension can also result in a monotonic effect on the generated rope. Regarding the effect of initial tension angle α , we have the following Lemma 5. In other word, with a fixed \hat{Q}_0 , i.e., fixed value of $r_1 Q_0 \sin(\varphi_1 - \alpha)$, a larger initial tension angle α results in a rope shape closer to the center \mathbf{D}_0 .

Lemma 5: *With a fixed value of \hat{Q}_0 (not Q_0) in the initial tension \mathbf{Q}_0 , in the generated rope shape $\{r(s), \varphi(s)\}$, $\forall \varphi_0 > \varphi_1$, the corresponding $r(s)$ when $\varphi(s) = \varphi_0$ is monotonically decreasing with respect to the tension angle $\alpha \in (\varphi_1 - \pi, \varphi_1)$.*

Proof: According to the closed-form expression of generated rope shape in (53) and (55), we prove the lemma by distinguishing the following two cases.

Case I: When $\alpha \in (\varphi_1 - \pi, \varphi_1 - \frac{\pi}{2}]$, we have $\frac{dr(s)}{d\varphi(s)} \Big|_{s=0} \geq 0$, so that the relation (53) holds. Similarly, with a fixed value of \hat{Q}_0 , we have $\frac{dr(s)}{d\sin(\varphi_1 - \alpha)}$ described as

$$\frac{dr(s)}{d\sin(\varphi_1 - \alpha)} = - \frac{H_1(\hat{Q}_0, \alpha, r_1, r(s))}{\frac{1}{r(s) \sqrt{\left(\frac{\rho_{\min}}{\hat{Q}_0} r(s) \int_{r_1}^{r(s)} g(r'_0) dr'_0 + \frac{r(s)}{r_1} \frac{1}{\sin(\varphi_1 - \alpha)} \right)^2 - 1}}} \quad (65)$$

where the expression $H_1(\hat{Q}_0, \alpha, r', r'')$ is defined as (66), shown at the bottom of the page. Therefore, when $\varphi(s) = \varphi_0 > \varphi_1$, we have $r(s) > r_1$ and accordingly $\frac{dr(s)}{d\sin(\varphi_1 - \alpha)} < 0$, i.e.,

$$\frac{dr(s)}{d\alpha} = \frac{dr(s)}{d\sin(\varphi_1 - \alpha)} (-\cos(\varphi_1 - \alpha)) < 0. \quad (67)$$

Case II: When $\alpha \in (\varphi_1 - \frac{\pi}{2}, \varphi_1)$, we have (55) holds. If $\varphi_0 > \varphi_1$ makes $\frac{dr(s)}{d\varphi(s)} \Big|_{\varphi(s)=\varphi_0} \leq 0$, according to (55), when $\varphi(s) = \varphi_0$, $\frac{dr(s)}{d\sin(\varphi_1 - \alpha)}$ can be obtained to be the same form as (65). Differently, we have $r(s) < r_1$, which results in $\frac{dr(s)}{d\sin(\varphi_1 - \alpha)} > 0$, namely $\frac{dr(s)}{d\alpha} < 0$ since $\cos(\varphi_1 - \alpha) > 0$ holds for $\alpha \in (\varphi_1 - \frac{\pi}{2}, \varphi_1)$.

If $\varphi_0 > \varphi_1$ makes $\frac{dr(s)}{d\varphi(s)} \Big|_{\varphi(s)=\varphi_0} > 0$, according to (55), when $\varphi(s) = \varphi_0$, with a fixed \hat{Q}_0 , $\frac{dr(s)}{d\sin(\varphi_1 - \alpha)}$ can be obtained as

$$\frac{dr(s)}{d\sin(\varphi_1 - \alpha)} = - \frac{H_2(\hat{Q}_0, \alpha, r(s)) + H_1(\hat{Q}_0, \alpha, 2r(s), r(s))}{\frac{1}{r(s) \sqrt{\left(\frac{\rho_{\min}}{\hat{Q}_0} r(s) \int_{r_1}^{r(s)} g(r'_0) dr'_0 + \frac{r(s)}{r_1} \frac{1}{\sin(\varphi_1 - \alpha)} \right)^2 - 1}}} \quad (68)$$

where the function $H_2(\hat{Q}_0, \alpha, r(s))$ is defined as

$$\begin{aligned} H_2(\hat{Q}_0, \alpha, r(s)) &= \frac{-2 \frac{dr_{\min}}{d\sin(\varphi_1 - \alpha)}}{r_{\min} \sqrt{\left(\frac{\rho_{\min}}{\hat{Q}_0} r_{\min} \int_{r_1}^{r_{\min}} g(r'_0) dr'_0 + \frac{r_{\min}}{r_1} \frac{1}{\sin(\varphi_1 - \alpha)} \right)^2 - 1}} \\ &\quad + H_1(\hat{Q}_0, \alpha, r_{\min}, r_1) + H_1(\hat{Q}_0, \alpha, r_{\min}, 2r(s)), \quad (69) \\ \frac{dr_{\min}}{d\sin(\varphi_1 - \alpha)} &= \frac{\frac{r_{\min}}{r_1} \frac{1}{\sin^2(\varphi_1 - \alpha)}}{\frac{1}{r_{\min}} + \frac{\rho_{\min}}{\hat{Q}_0} r_{\min} g(r_{\min})} > 0. \quad (70) \end{aligned}$$

Following the same process in the proof of Lemma 4, by introducing $z(r)$ in (62) and a variable ϵ , we can find that $H_2(\hat{Q}_0, \alpha, r(s)) \leq 0$. Since $H_1(\hat{Q}_0, \alpha, 2r(s), r(s)) < 0$ holds, we can obtain that $\frac{dr(s)}{d\sin(\varphi_1 - \alpha)} > 0$ holds for given \hat{Q}_0 . Subsequently, we obtain that $\frac{dr(s)}{d\alpha} < 0$ for any given \hat{Q}_0 .

To sum up, for any given fixed \hat{Q}_0 , it holds that $\frac{dr(s)}{d\alpha} < 0$, $\forall \alpha \in (\varphi_1 - \pi, \varphi_1)$, i.e., $r(s)$ is strictly monotonically decreasing with respect to α . \square

D. Relation Between α and Total Rope Length

Based on Lemma 4 and Lemma 5 which respectively show the monotonic effects of initial tension value Q_0 and initial tension angle α on the generated shape, we can obtain a monotonic relation between the tension angle α and the total rope length S . This relation is described in Lemma 6.

Lemma 6: *When the tension value is $Q_0 = Q_0^*(\alpha)$, so that the generated rope shape $(r(s), \varphi(s))$ starts from $\mathbf{D}_1(r_1, \varphi_1)$ and ends at $\mathbf{D}_2(r_2, \varphi_2)$, the total rope length between \mathbf{D}_1 and \mathbf{D}_2 is strictly monotonically increasing with respect to α .*

Proof: We prove the lemma in the following way with three steps: i. first propose a concept of unlimited rope shape, then ii. find the relation between generated ropes with the same endpoints with the assistance of unlimited rope shape (namely no further intersection points between different generated ropes with the same endpoints), and iii. finally complete the proof based on a property of convex bodies.

We start with introducing the concept of unlimited rope shape. Note that given an initial tension \mathbf{Q}_0 at point \mathbf{D}_1 , the rope shape can be generated on both left side and right side of line $\mathbf{D}_0\mathbf{D}_1$. More specifically, for the sides $\varphi > \varphi_1$ and $\varphi < \varphi_1$, the balanced rope shapes can be generated respectively with initial rope tensions \mathbf{Q}_0 and $-\mathbf{Q}_0$. An example of created unlimited rope shape is shown in Fig. 7(a). In other words, with any given initial rope tension \mathbf{Q}_0 , a unique smooth rope shape without endpoints can be correspondingly created.

Then, we prove a statement that for any two different created unlimited rope shapes, there are at most two intersection points. We assume two created unlimited rope shapes have an intersection point $\mathbf{D}_3(r_3, \varphi_3)$, and the corresponding two rope tensions at \mathbf{D}_3 are respectively \mathbf{Q}_1 and \mathbf{Q}_2 with their

$$H_1(\hat{Q}_0, \alpha, r', r'') = \int_{r'}^{r''} \frac{\left(\frac{\rho_{\min}}{\hat{Q}_0} r_0 \int_{r_1}^{r_0} g(r'_0) dr'_0 + \frac{r_0}{r_1} \frac{1}{\sin(\varphi_1 - \alpha)} \right) \left(\frac{r_0}{r_1} \frac{1}{\sin^2(\varphi_1 - \alpha)} \right)}{r_0 \left(\sqrt{\left(\frac{\rho_{\min}}{\hat{Q}_0} r_0 \int_{r_1}^{r_0} g(r'_0) dr'_0 + \frac{r_0}{r_1} \frac{1}{\sin(\varphi_1 - \alpha)} \right)^2 - 1}} \right)^3} dr_0 \quad (66)$$

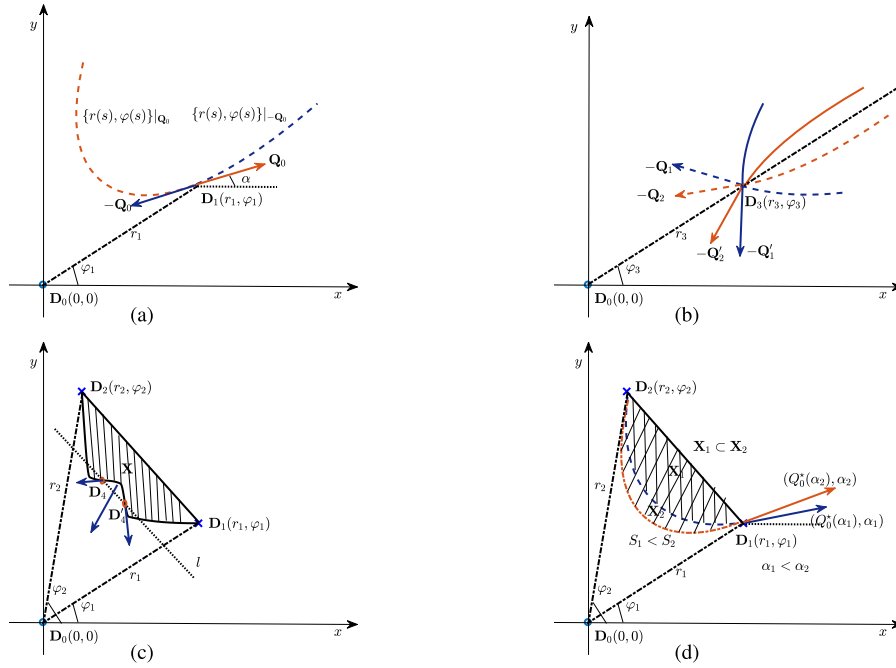


Fig. 7. Example figures for proof of Lemma 6. (a) An example of creating unlimited rope shape. (b) An example of symmetry. (c) An example of unbalanced rope segment within non-convex area X . (d) Effect of initial angle α on the total rope length S .

tensions Q_1, Q_2 and angles $\alpha_1, \alpha_2 \in (\varphi_3 - \pi, \varphi_3)$, $\alpha_1 \leq \alpha_2$. Accordingly, we have $\hat{Q}_1 = r_3 Q_1 \sin(\varphi_3 - \alpha_1)$ and $\hat{Q}_2 = r_3 Q_2 \sin(\varphi_3 - \alpha_2)$. Then, we show that there is no intersection point in at least one side, i.e., in either the side of $\varphi > \varphi_3$ or $\varphi < \varphi_3$. In particular, we show this by distinguishing the following these cases satisfying $\alpha_1 \leq \alpha_2$.

- If $\alpha_1 < \alpha_2$ and $\hat{Q}_1 \leq \hat{Q}_2$ ($Q_1 \leq \frac{Q_2 \sin(\varphi_3 - \alpha_2)}{\sin(\varphi_3 - \alpha_1)}$), according to Lemma 4 and Lemma 5, we have that given $\varphi > \varphi_3$, the corresponding distance r satisfies

$$r|_{(\alpha_2, Q_2)} \stackrel{\text{Lemma 5}}{<} r|_{(\alpha_1, \frac{Q_2 \sin(\varphi_3 - \alpha_2)}{\sin(\varphi_3 - \alpha_1)})} \stackrel{\text{Lemma 4}}{\leq} r|_{(\alpha_1, Q_1)}. \quad (71)$$

Therefore, there is no intersection point in the rope shapes generated from initial tensions Q_1 and Q_2 , i.e., at the side of $\varphi > \varphi_3$.

- If $\alpha_1 < \alpha_2$ and $\hat{Q}_1 > \hat{Q}_2$, we study the side where $\varphi < \varphi_3$, namely the generated rope segment from initial tensions $-Q_1$ and $-Q_2$. As the angles of initial tensions are located out of the interval $(\varphi_3 - \pi, \varphi_3)$, we have that the relations (53) and (55) do not hold any more. However, due to the symmetry of force field (20), we can directly focus on the generated rope from tensions $-Q'_1(\alpha'_1 = 2\varphi_3 - \alpha_1 - \pi, Q_1)$ and $-Q'_2(\alpha'_2 = 2\varphi_3 - \alpha_2 - \pi, Q_2)$, as implied in Fig. 7(b). Clearly, $\alpha'_1 > \alpha'_2$. Thus, for given $\varphi > \varphi_3$,

$$r|_{(\alpha'_2, Q_2)} \stackrel{\text{Lemma 5}}{>} r|_{(\alpha'_1, \frac{Q_2 \sin(\varphi_3 - \alpha'_2)}{\sin(\varphi_3 - \alpha'_1)})} \stackrel{\text{Lemma 4}}{>} r|_{(\alpha'_1, Q_1)}. \quad (72)$$

According to the symmetry, we can conclude that there is no intersection point in the rope shapes generated from initial tensions $-Q_1$ and $-Q_2$, i.e., at the side of $\varphi < \varphi_3$.

- If $\alpha_1 = \alpha_2$, it must hold that $Q_1 \neq Q_2$, otherwise Q_1 and Q_2 will generate totally same rope shape. As $Q_1 \neq Q_2$,

the two created rope shape has no intersection as the side of $\varphi > \varphi_3$ according to Lemma 4.

Hence, the statement “for any two different created unlimited rope shapes, there are at most two intersection points” can be immediately proved by contradiction. In particular, if there are more than two intersection points of two different created unlimited rope shapes, as discussed, the two rope shapes must have the same tensions at one of the intersection point so that these two rope shapes are exactly the same one.

Next, we discuss two initial tensions, i.e., $(\alpha_1, Q_0^*(\alpha_1))$ and $(\alpha_2, Q_0^*(\alpha_2))$ ($\alpha_1 < \alpha_2$), at point D_1 . Clearly, both two generated ropes pass through points D_1 and D_2 . According to the proved statement, there is no other intersection point between D_1 and D_2 , namely no intersection point when $\varphi \in (\varphi_1, \varphi_2)$. On the other hand, the initial value of $\frac{dr(s)}{d\varphi(s)}$ is determined by α , i.e., $\frac{dr(s)}{d\varphi(s)} \Big|_{s=0} = -\frac{r_1}{\tan(\varphi_1 - \alpha)}$. As $\alpha_1 < \alpha_2$ results in $-\frac{r_1}{\tan(\varphi_1 - \alpha_1)} > -\frac{r_1}{\tan(\varphi_1 - \alpha_2)}$, we have

$$r(s)|_{(\alpha_1, Q_0^*(\alpha_1))} > r(s)|_{(\alpha_2, Q_0^*(\alpha_2))}, \text{ when } \varphi(s) \in (\varphi_1, \varphi_2). \quad (73)$$

We denote by X_1 the area constructed by the line segment $D_1 D_2$ and the rope segment generated by initial tension $(\alpha_1, Q_0^*(\alpha_1))$, while X_2 is the area corresponding to initial tension $(\alpha_2, Q_0^*(\alpha_2))$, as shown in Fig. 7(d). Therefore, the area X_1 is a proper subset of X_2 , i.e., $X_1 \subsetneq X_2$. In particular, the intersection of X_1 and any straight line is convex, otherwise we can find a rope segment which is not in the state of equilibrium, e.g., the rope segment $D_4 D'_4$ in Fig. 7(c). The same conclusion holds for X_2 . Thus, both X_1 and X_2 are convex sets.

According to the geometry property of convex sets [28], we have the perimeter of X_2 is larger than that of X_1 when $X_1 \subsetneq X_2$. The perimeters of X_1 and X_2 are actually the

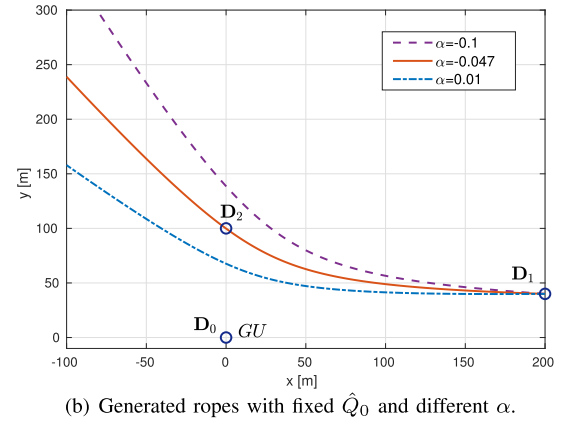
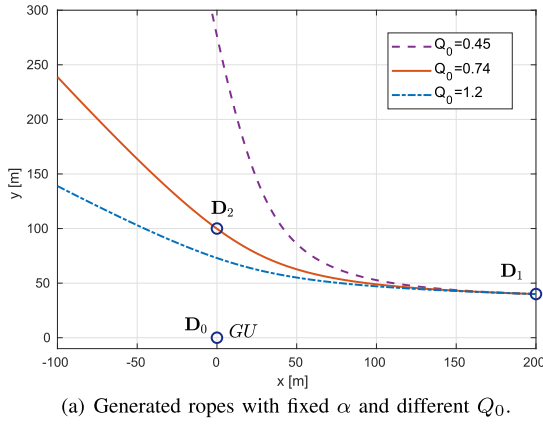


Fig. 8. Observations of the monotonic impact of absolute value Q_0 and angle α in initial tension.

rope length between D_1 and D_2 plus the length of line segment D_1D_2 . Therefore, we obtain that for any two initial tensions, $(\alpha_1, Q_0^*(\alpha_1))$ and $(\alpha_2, Q_0^*(\alpha_2))$, if $\alpha_1 < \alpha_2$ holds, we always have the total rope length corresponding to initial tension $(\alpha_2, Q_0^*(\alpha_2))$ is larger than that of $(\alpha_1, Q_0^*(\alpha_1))$, i.e., $S_2 > S_1$. \square

Therefore, according to Lemma 6, while keeping $Q_0 = Q_0^*(\alpha)$, we can find a unique angle α^* by tuning the value of α , so that the length of generated rope between D_1 and D_2 is exactly equal to $S^* = \frac{m}{\rho_{\min}}$. Combining the optimal tension angle α^* and the corresponding optimal tension value $Q_0^*(\alpha^*)$, the optimal initial tension Q_0^* can be uniquely constructed, and subsequently we can build the optimal rope solution for (P3) in case of $m < \rho_{\min}(r_1 + r_2)$, equivalently the optimal UAV trajectory for (OP) in case of $T < \frac{r_1+r_2}{V}$.

Immediately, we conclude that the optimal rope shape $\{r^*(s), \varphi^*(s)\}$ generated by the optimal initial tension Q_0^* satisfies the following two conditions:

- (i). $\{r^*(s), \varphi^*(s)\}$ passes through the point $D_2(r_2, \varphi_2)$;
- (ii). The total rope length of $\{r^*(s), \varphi^*(s)\}$ is $\frac{m}{\rho_{\min}}$.

As a unique Q_0 can be found while satisfying these two conditions, the found Q_0 must be the optimal initial tension, so that the obtained rope solution and equivalent trajectory solution are absolutely optimal.

VI. SIMULATION RESULTS

In this section, via simulation results, we validate the monotonic impacts of the absolute value Q_0 and angle α on the generated rope, and evaluate our globally optimal design by comparing the obtained optimal trajectory with the solution from existing trajectory design strategies. The simulation setups are initialized as: $H = 10\text{m}$, $\frac{\beta P}{\sigma^2} = 80\text{dB}$, $D_0 = (0, 0)\text{m}$, $D_1 = (200, 40)\text{m}$ and $D_2 = (0, 100)\text{m}$.

At first, with a fixed angle $\alpha = -0.047$, the effect of absolute tension Q_0 is depicted in Fig. 8(a). We observe that a larger Q_0 makes the generated rope closer to D_0 , while decreasing Q_0 leads to an upward movement of the generated rope. This indicates a unique Q_0 can be found resulting in a generated rope passing through D_2 . From the figure, with our simulation setup, the optimal Q_0 is clearly equal to 0.74 when $\alpha = -0.047$. The correctness of the proved Lemma 4 is

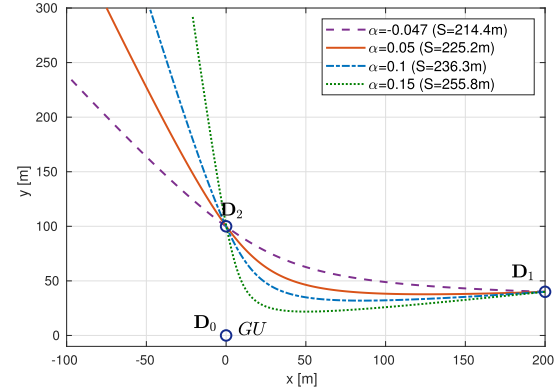


Fig. 9. Generated ropes with different α and optimized $Q_0 = Q_0^*(\alpha)$.

therefore confirmed. Next, in Fig. 8(b), we show the effect of α on the generated rope with a fixed $\hat{Q}_0 = 40.461$. Clearly, with different initial tension angle α , the initial curve slope at D_1 , which is directly influenced by α , becomes different. Besides, we can also observe that the generated rope becomes closer to D_0 when α increases. The Lemma 5 of monotonic effect of angle α is thus confirmed.

Then, with $Q_0 = Q_0^*(\alpha)$ which guarantees the generated rope passing through D_2 , we study the behaviour of the generated rope with varying tension angle α in Fig. 9. Clearly illustrated, when Q_0 guarantees the rope passing through D_2 , the rope segment between D_1 and D_2 tends to be expanded towards the direction to D_0 . Note that the rope lengths of segment between D_1 and D_2 with different initial angle α have been calculated and listed in the legend. By comparing the length of rope segment, we can find that the rope length S is monotonically increasing with respect to the initial tension angle α . As a result, the conclusion in Lemma 6 is also confirmed. Therefore, via greedily searching, our design for insufficient rope mass m , i.e., insufficient time duration T , is capable of finding the optimal initial rope tension and resulting a global optimal UAV trajectory.

Furthermore, we validate the optimality of our design (i.e., **global optimal**) by comparing it with two existing efficient trajectory design strategies:

- **successive convex programming (SCP)-based design:**

As a popular strategy, the SCP-based design quantizes

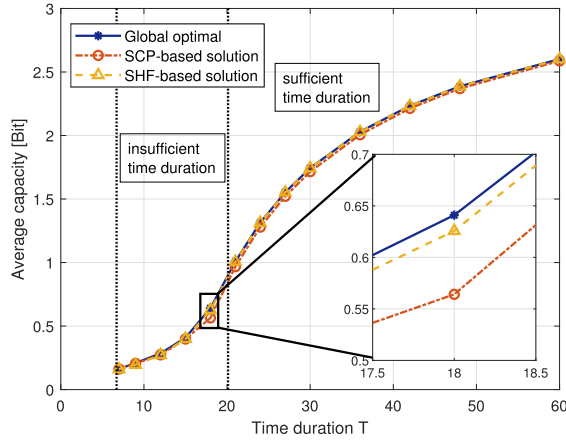


Fig. 10. Performance comparison with different time duration T .

the trajectory over time with a resolution δT . The value of δT is assumed to be sufficiently small, so that the UAV can be considered to be static in a time slot with length δT . Then by dividing the UAV trajectory into $\frac{T}{\delta T}$ time slots and optimizing the UAV positions in all time slots via SCP techniques, a suboptimal UAV trajectory can be obtained. However, note that the SCP-based design can only obtain a discretized solution, which is required to be modified before realistic applications. Generally, the trajectory is modified by letting the UAV fly between discrete points with a uniform speed along a straight line. The speed is dependent on the distance between these discrete points and the time resolution. For an accurate comparison, we evaluate the corresponding performance based on the modified realistic trajectory.

- **successive-hover-fly (SHF)-based design:** In the SHF structure, the UAV will successively visit all hovering points and fly along a straight line with maximum speed V in each two neighbour hovering points. For comparison, we construct the SHF-based design in our problem (OP) with a single hovering point. The UAV flies from \mathbf{D}_1 to a designed hovering point and back to \mathbf{D}_2 along straight lines with a hovering behaviour at the hovering point. In simulations, we find the defined hovering points and hovering duration via exhaustive search.

The default simulation setups for the comparison with existing strategies are as following: $H = 10\text{m}$, $\frac{\beta P}{\sigma^2} = 30\text{dB}$, $\mathbf{D}_0 = (0, 0)\text{m}$, $\mathbf{D}_1 = (100, 50)\text{m}$ and $\mathbf{D}_2 = (40, 80)\text{m}$, which can provide us a better view of the differences in trajectories designed by different strategies. We depict in Fig. 10 the average capacity obtained from all three strategies with varying time duration T and in Fig. 11 the corresponding computational CPU time for the complexity comparison. From Fig. 10, clearly, a larger time duration T results in a higher average capacity for all strategies, which confirms the benefits of allocating more time resource to the communication task. By comparing the network performance in the enlarged figure, we find that our proposed solution always outperforms the two benchmarks, which validates the optimality of our proposed solution. On the other hand, by observing Fig. 11, we observe that our proposed solution also shows an extremely lower

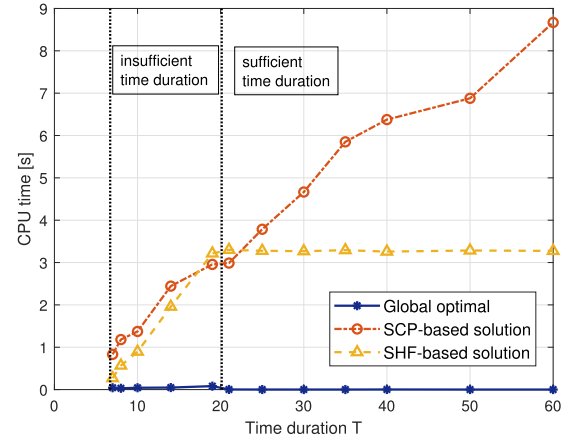


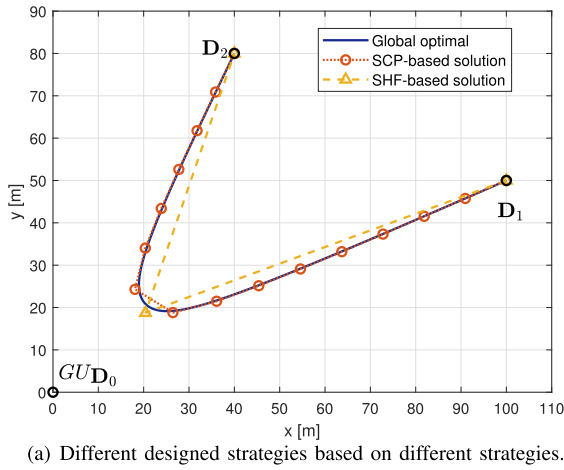
Fig. 11. Computational complexity comparison with different time duration T .

complexity compared to the two benchmarks, especially when the time duration T is relatively larger. This is due to the fact that we have built a closed-form expression for the optimal trajectory. Note that the complexity of SHF-based solution results from the exhaustive search of the hovering points. With relatively smaller T , the feasible region of hovering points tends to be smaller and leads to a lower complexity.

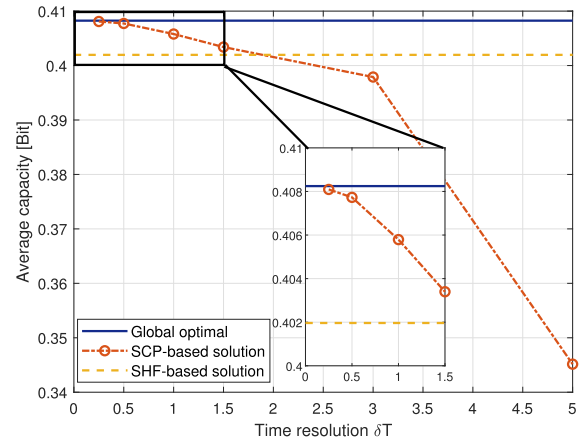
Finally, in Fig. 12(a), we show the results of different designed UAV trajectory from different strategies. We observe that the discrete points from SCP-based design are located much closer to the global optimal solution, which results from our proposed design. However, the modification (straight lines between discrete points) on SCP-based design for forming a continuous trajectory still makes the solution deviate from the optimal one. As for SHF-based design, the difference compared to the optimal solution obviously comes from the assumption of straight lines between hovering points, which is not optimal.

Then, we depict the average capacity of three designs, i.e., $\frac{U(\{x(t), y(t)\})}{BT}$, in Fig. 12(b) for the system performance evaluation. Apparently, with higher time resolution (smaller δT), the discretization errors in SCP-based design are reduced, so that a better average channel capacity, also a larger overall throughput, can be obtained. Although, the performance of SCP-based design is still upper bounded by that of our proposed solution, which further confirms the global optimality of our design. On the other hand, a higher resolution, a smaller δT , will also increase the number of variables to be optimized, which will lead to a higher complexity. By comparison, our proposed design is based on a closed-form expression which provides an absolutely lower complexity. Moreover, the SHF-based design is also below the optimal one and becomes even better than the result from SCP-based design with a lower time resolution.

Remark 2: Note that it should be mentioned that SCP-based design requires a convex approximation of the quantized problem, which is much likely inaccessible in a scenario with complex models. By contrast, the derivations in our proposed strategy for single-user network only requires a monotonic increasing property (Property 1) on APF, i.e., position closer to user has a better performance, which can be easily satisfied



(a) Different designed strategies based on different strategies.



(b) Performance comparison of different strategies.

Fig. 12. Comparison of different strategies.

in most scenarios, like the scenario with probabilistic LoS model. Therefore, our proposed strategy is again demonstrated to have a high capability in extensions. In particular, for single-user networks, as long as the Property 1 holds for the corresponding APF, the global optimality of extended solution can also be guaranteed. For multi-user networks, this novel strategy can also enable the corresponding characterization and make the optimal solution analyzable.

VII. CONCLUSION

In this paper, we proposed a novel strategy for optimally designing the UAV trajectory. We first introduce the mechanical concept of APF into trajectory design and consider a single-user network as an example network for strategy clarification. By representing the opposite of the objective in design with artificial potential energy, the trajectory design problem is reformulated to a mechanical problem, namely a shape design of a rope in equilibrium. In the considered network, the optimal rope shape is investigated via mechanical principles. Different approaches are provided for obtaining the optimal solution to the problems under different assumptions of rope mass. The optimal UAV trajectory is equivalently constructed from the optimal rope shape. The optimality of obtained solution is further confirmed by the simulation results. It is worthwhile to mention that a **close-form expression** of the globally optimal **curving** trajectory is for the first time provided, which is expected to open a door for researchers in this area handling similar/related problems.

As for potential extensions, by defining a different APF according to the objective, our proposed novel strategy can be directly extended into various UAV systems with obstacle avoidance, different channel and topology models, user numbers, design objectives, UAV tasks and so on, which confirms the high adaptability. More specifically, when the user has a continuously changing location, we can still model the user mobility into a conditionally varying APF and construct the equivalent physical problem. For the scenario where the acceleration limit is necessary to be considered, we can also model the limit as a constraint on the curvature and line density variation in the equivalent physical problem. By combining multiple APFs from different users into one integrated APF,

the trajectory design problem in multi-user scenario also becomes possible to be analyzed in physics domain.

Moreover, it should be pointed out that in comparison to traditional trajectory design, the complexity of calculating the UAV trajectory based on the close-form expression is negligible. Hence, applying learning process (even the time-consuming deep reinforcement learning) on the UAV become highly possible, which could handle the UAV network serving dynamic GUs, where the number and locations of the users changes in a quasi-static manner. We finalize the work by stressing that via the introduced equivalence to mechanical problems, not only the mechanical principles, but also the physics simulation softwares, e.g., *Interactive physics* and *QuickField* which allow to self-define a force field, highly probably become efficient tools in the design of UAV trajectories.

APPENDIX A PROOF OF LEMMA 1

In the rope defined by (22), (23) and (24), the total mass m is divided into three parts, i.e., mass $\rho_{\min}r_1$ and $\rho_{\min}r_2$ on two straight lines I^* and III^* , and a mass point II^* with mass $m - \rho_{\min}(r_1 + r_2)$ at D_0 , as marked in Fig. 13(a). For any feasible solution $\{\hat{x}'_0(s), \hat{y}'_0(s)\}$, $\rho_0(s)$ and S_0 to problem (P3), starting with D_1 , we can accordingly cut it into three segments I, II and III, respectively with mass $\rho_{\min}r_1$, $m - \rho_{\min}(r_1 + r_2)$ and $\rho_{\min}r_2$. An example of cutting a feasible solution is shown in Fig. 13(a). Hence, the optimality of the solution can be shown by proving that the potential energy of each segment $i \in \{I, II, III\}$ in the feasible solution is lower-bounded by that of corresponding segment i^* . According to the monotonic Property 1 of APF, the point D_0 has the lowest potential in the whole field, i.e., the potential energy of segment II^* is definitely lower than or equal to the one of segment II. Hence, the remaining tasks are the proof for segment I and segment II.

Let us then consider segment I and denote by s_1 the corresponding total length. In particular, for a subsegment in I which starts from D_1 and has a length of s , we denote by $U_I(s)$ and $m_I(s)$ the potential energy and mass of this subsegment. An example of such subsegment is shown in Fig. 13(b). Hence,

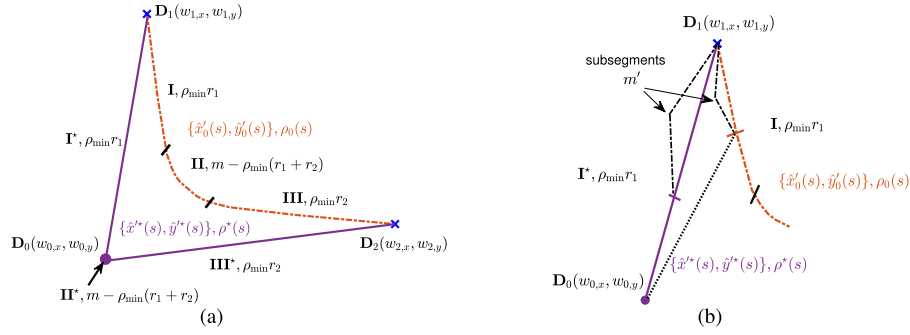


Fig. 13. Figures for Proof 1. (a) An example of optimal solution and feasible solution with sufficient rope mass. (b) An example of subsegments in I and I^* .

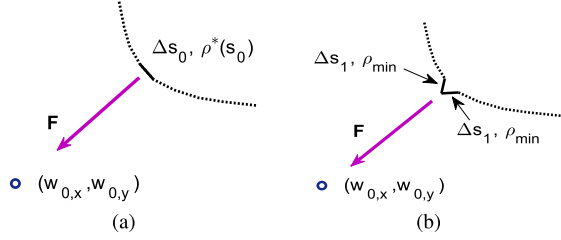


Fig. 14. For proof of density property. (a) An example for a sufficiently short segment. (b) Modification with lower potential energy.

we have

$$U_I(s) = \int_0^s R''(\hat{x}'_0(s'), \hat{y}'_0(s')) \rho_0(s') ds', \quad s \in [0, s_1], \quad (74)$$

$$m_I(s) = \int_0^s \rho_0(s') ds', \quad s \in [0, s_1]. \quad (75)$$

Immediately, we have the potential energy of segment I given by $U_I(s_1)$ and $m_I(s_1) = \rho_{\min} r_1$.

Correspondingly, we can also define by s_{I^*} , $U_{I^*}(s)$ and $m_{I^*}(s)$ the total length of for segment I^* , the potential energy and mass of a subsegment in segment I^* . According to the definition of potential energy and mass of the subsegment, we can formulate the following relations in differentiation

$$\frac{dU_I(s)}{dm_I(s)} = R''(\hat{x}'_0(s), \hat{y}'_0(s)), \quad \frac{dU_{I^*}(s)}{dm_{I^*}(s)} = R''(\hat{x}'^*(s), \hat{y}'^*(s)). \quad (76)$$

Note that for a given value of $m_I(s) = m' \in [0, \rho_{\min} r_1]$, the distance from the other end $(\hat{x}'_0(s), \hat{y}'_0(s))$ of the subsegment in I to D_0 is lower-bounded by $\frac{\rho_{\min} r_1 - m'}{\rho_{\min}} = r_1 - \frac{m'}{\rho_{\min}}$, while this lower-bound is exactly the distance from the other end of the subsegment in I^* to D_0 when $m_{I^*}(s) = m'$, as implied in Fig. 13(b). According to Property 1 which shows that APF $R''(x, y)$ is monotonic increasing with respect to distance $r(x, y)$, we can conclude that when $m_I(s) = m_{I^*}(s) = m' \in [0, \rho_{\min} r_1]$, $\frac{dU_I(s)}{dm_I(s)}|_{m_I(s)=m'} \geq \frac{dU_{I^*}(s)}{dm_{I^*}(s)}|_{m_{I^*}(s)=m'}$ holds. As $m_I(0) = m_{I^*}(0) = 0$, $m_I(s_1) = m_{I^*}(s_{I^*}) = \rho_{\min} r_1$ and $U_I(0) = U_{I^*}(0) = 0$ hold, we have $U_I(s_1) \geq U_{I^*}(s_{I^*})$, namely segment I^* possesses lower potential energy than segment I. Similarly, we have the potential energy of segment III^* is lower than that of segment III.

Thus, for any feasible solution to (P3), the corresponding potential energy is not lower than that of the solution defined

by (22), (23) and (24), i.e., the optimality of the constructed solution is proven.

APPENDIX B PROOF OF LEMMA 2

We prove the lemma by contradiction. Assume that in the optimal rope solution $\{\hat{x}'^*(s), \hat{y}'^*(s)\}, \rho^*(s)$ and S'^* of problem (P3), $\exists s_0 \in [0, S'^*]$ such that $(\hat{x}'^*(s_0), \hat{y}'^*(s_0)) \neq D_0 = (w_{0,x}, w_{0,y})$ and $\rho^*(s_0) > \rho_{\min}$. Then, we select a sufficiently short segment Δs_0 around s_0 , such that the line density in the segment Δs_0 can be considered as a constant $\rho^*(s_0)$, as shown in Fig. 14(a). And we can construct two rope segments with line density ρ_{\min} and length $\Delta s_1 = \frac{1}{2} \frac{\rho^*(s_0)}{\rho_{\min}} \Delta s_0$. The total mass of the two introduced segments Δs_1 is the same as that of segment Δs_0 . Thus, by replacing Δs_0 with two segments Δs_1 , as shown in Fig. 14(b), the total mass of the rope is not affected. Clearly, we have $2\Delta s_1 = \frac{\rho^*(s_0)}{\rho_{\min}} \Delta s_0 > \Delta s_0$, which implies that the segment length $2\Delta s_1$ is enough to connect the rope. Furthermore, as segments Δs_1 are obviously closer to the point D_0 than segment Δs_0 , a reduction on the artificial potential energy is observed in the replacement behavior, according to the monotonic Property 1 of APF. Therefore, a rope solution with better objective for (P3) is constructed in Fig. 14(b), which is contradict to the assumption of the optimal rope solution.

REFERENCES

- [1] L. Gupta, R. Jain, and G. Vaszkun, "Survey of important issues in UAV communication networks," *IEEE Commun. Surveys Tuts.*, vol. 18, no. 2, pp. 1123–1152, 2nd Quart., 2016.
- [2] T. Tomic *et al.*, "Toward a fully autonomous UAV: Research platform for indoor and outdoor urban search and rescue," *IEEE Robot. Autom. Mag.*, vol. 19, no. 3, pp. 46–56, Sep. 2012.
- [3] N. H. Motlagh, M. Bagaa, and T. Taleb, "UAV-based IoT platform: A crowd surveillance use case," *IEEE Commun. Mag.*, vol. 55, no. 2, pp. 128–134, Feb. 2017.
- [4] H. Hellaoui, O. Bekkouche, M. Bagaa, and T. Taleb, "Aerial control system for spectrum efficiency in UAV-to-cellular communications," *IEEE Commun. Mag.*, vol. 56, no. 10, pp. 108–113, Oct. 2018.
- [5] M. Cui, G. Zhang, Q. Wu, and D. W. K. Ng, "Robust trajectory and transmit power design for secure UAV communications," *IEEE Trans. Veh. Technol.*, vol. 67, no. 9, pp. 9042–9046, Sep. 2018.
- [6] Y. Zeng, R. Zhang, and T. J. Lim, "Wireless communications with unmanned aerial vehicles: Opportunities and challenges," *IEEE Commun. Mag.*, vol. 54, no. 5, pp. 36–42, May 2016.
- [7] X. Zhang and L. Duan, "Optimization of emergency UAV deployment for providing wireless coverage," in *Proc. GLOBECOM*, Singapore, Dec. 2017, pp. 1–6.
- [8] J. Lyu, Y. Zeng, R. Zhang, and T. J. Lim, "Placement optimization of UAV-mounted mobile base stations," *IEEE Commun. Lett.*, vol. 21, no. 3, pp. 604–607, Mar. 2017.

- [9] M. Alzenad, A. El-Keyi, and H. Yanikomeroglu, "3-D placement of an unmanned aerial vehicle base station for maximum coverage of users with different QoS requirements," *IEEE Wireless Commun. Lett.*, vol. 7, no. 1, pp. 38–41, Feb. 2018.
- [10] Y. Chen, W. Feng, and G. Zheng, "Optimum placement of UAV as relays," *IEEE Commun. Lett.*, vol. 22, no. 2, pp. 248–251, Feb. 2018.
- [11] P. Li and J. Xu, "Fundamental rate limits of UAV-enabled multiple access channel with trajectory optimization," *IEEE Trans. Wireless Commun.*, vol. 19, no. 1, pp. 458–474, Jan. 2020.
- [12] Q. Wu, J. Xu, and R. Zhang, "Capacity characterization of UAV-enabled two-user broadcast channel," *IEEE J. Sel. Areas Commun.*, vol. 36, no. 9, pp. 1955–1971, Sep. 2018.
- [13] Y. Zeng, R. Zhang, and T. J. Lim, "Throughput maximization for UAV-enabled mobile relaying systems," *IEEE Trans. Commun.*, vol. 64, no. 12, pp. 4983–4996, Dec. 2016.
- [14] Y. Zeng, J. Xu, and R. Zhang, "Energy minimization for wireless communication with rotary-wing UAV," *IEEE Trans. Wireless Commun.*, vol. 18, no. 4, pp. 2329–2345, Apr. 2019.
- [15] C. Zhan and H. Lai, "Energy minimization in Internet-of-Things system based on rotary-wing UAV," *IEEE Wireless Commun. Lett.*, vol. 8, no. 5, pp. 1341–1344, Oct. 2019.
- [16] Y. Zeng and R. Zhang, "Energy-efficient UAV communication with trajectory optimization," *IEEE Trans. Wireless Commun.*, vol. 16, no. 6, pp. 3747–3760, Jun. 2017.
- [17] C. Zhan, Y. Zeng, and R. Zhang, "Energy-efficient data collection in UAV enabled wireless sensor network," *IEEE Wireless Commun. Lett.*, vol. 7, no. 3, pp. 328–331, Jun. 2018.
- [18] Y. Zeng, X. Xu, and R. Zhang, "Trajectory design for completion time minimization in UAV-enabled multicasting," *IEEE Trans. Wireless Commun.*, vol. 17, no. 4, pp. 2233–2246, Apr. 2018.
- [19] Y. Hu, X. Yuan, J. Xu, and A. Schmeink, "Optimal 1D trajectory design for UAV-enabled multiuser wireless power transfer," *IEEE Trans. Commun.*, vol. 67, no. 8, pp. 5674–5688, Aug. 2019.
- [20] M. E. Gurtin, *An Introduction to Continuum Mechanics*. New York, NY, USA: Academic, 1982.
- [21] M. G. Park, J. H. Jeon, and M. C. Lee, "Obstacle avoidance for mobile robots using artificial potential field approach with simulated annealing," in *Proc. IEEE ISIE*, vol. 3, Jun. 2001, pp. 1530–1535.
- [22] Y.-B. Chen, G.-C. Luo, Y.-S. Mei, J.-Q. Yu, and X.-L. Su, "UAV path planning using artificial potential field method updated by optimal control theory," *Int. J. Syst. Sci.*, vol. 47, no. 6, pp. 1407–1420, Apr. 2016.
- [23] F. Cheng *et al.*, "UAV trajectory optimization for data offloading at the edge of multiple cells," *IEEE Trans. Veh. Technol.*, vol. 67, no. 7, pp. 6732–6736, Jul. 2018.
- [24] L. Xie, J. Xu, and R. Zhang, "Throughput maximization for UAV-enabled wireless powered communication networks," *IEEE Internet Things J.*, vol. 6, no. 2, pp. 1690–1703, Apr. 2019.
- [25] J. Xu, Y. Zeng, and R. Zhang, "UAV-enabled wireless power transfer: Trajectory design and energy optimization," *IEEE Trans. Wireless Commun.*, vol. 17, no. 8, pp. 5092–5106, Aug. 2018.
- [26] S. Pradhan and S. Sinha, *Analytical Statics*. New York, NY, USA: Academic, 2006.
- [27] V. F. Zaitsev and A. D. Polyaniin, *Handbook of Exact Solutions for Ordinary Differential Equations*. Boca Raton, FL, USA: CRC Press, 2002.
- [28] T. Bonnesen and W. Fenchel, *Theory of Convex Bodies*. Moscow, Russia: BCS Associates, 1987.



Xiaopeng Yuan (Graduate Student Member, IEEE) received the B.Sc. degree in automation from the Beijing University of Aeronautics and Astronautics, China, in 2016, and the M.Sc. degree in electrical engineering, information technology, and computer engineering from RWTH Aachen University, Germany, in 2019, where he is currently pursuing the Ph.D. degree. His research interests are in UAV-assisted wireless networks, wireless power transfer networks, ultra-reliable low-latency communication networks, and trajectory design and optimization technology.



Yulin Hu (Senior Member, IEEE) received the M.Sc.E.E. degree from USTC, China, in 2011, and the Ph.D.E.E. degree (Hons.) from RWTH Aachen University. He successfully defended his dissertation of the joint Ph.D. Program supervised by Prof. Anke Schmeink at RWTH Aachen University and Prof. James Gross at KTH Royal Institute of Technology in December 2015. Since January 2016 to December 2016, he has been a Post-Doctoral Research Fellow with RWTH Aachen University. He was a Senior Researcher and Team Leader with Prof. Anke Schmeink at ISEK Research Area, RWTH Aachen University. From May 2017 to July in 2017, he was a Visiting Scholar with Prof. M. Cen Gursoy at Syracuse University, USA. He is currently a Professor with the School of Electronic Information, Wuhan University, and an Adjunct Senior Researcher with ISEK Research Area, RWTH Aachen University. His research interests are in information theory and optimal design of wireless communication systems. He has been invited to contribute submissions to multiple conferences. He was a recipient of the IFIP/IEEE Wireless Days Student Travel Awards in 2012. He received the Best Paper Awards at IEEE ISWCS 2017 and IEEE PIMRC 2017. He served as a TPC member for many conferences. He was the Lead Editor of the Ullc-LoPIoT special issue in *Physical Communication*, and the Organizer and the Chair of two special sessions in IEEE ISWCS 2018 and ISWCS 2020. He is currently serving as an Editor for *Physical Communication* (Elsevier), *EURASIP Journal on Wireless Communications and Networking*, and *Frontiers in Communications and Networks*.



Deshi Li received the Ph.D. degree in computer application technology from Wuhan University, Wuhan, China. He was a Visiting Scholar with the Network Laboratory, University of California at Davis, Davis, CA, USA. He is currently a Professor with the Electronic Information School, Wuhan University. He is also an Associate Chief Scientist of Space Communication Area with the Collaborative Innovation Center for Geospatial Technology, Hubei, China. His recent research projects include the National Science and Technology Major Project of China (973 Program), the National High Technology Program of China (863 Program), and the National Natural Science Foundation of China. He has published over 100 research articles. His current research interests include wireless communication, the Internet of Things, intelligence systems, and SoC design. He serves as a reviewer for several international academic journals and an Expert Evaluator for the Ministry of Science and Technology of China, the Ministry of Education of China, and NSF China. He currently serves as a member of the Internet of Things Expert Committee and the Education Committee of the Chinese Institute of Electronics. He is an Executive Trustee Member of the China Cloud System Pioneer Strategic Alliance.



Anke Schmeink (Senior Member, IEEE) received the Diploma degree in mathematics (medicine) and the Ph.D. degree in electrical engineering and information technology from RWTH Aachen University, Germany, in 2002 and 2006, respectively. Before joining the RWTH Aachen University in 2008, she worked as a Research Scientist for Philips Research. Since 2012, she has been a Professor with RWTH Aachen University. She spent several research visits with the University of Melbourne and University of York. Her research interests are in information theory, machine learning, data analytics, and optimization with a focus on wireless communications and medical applications. She is a member of the Young Academy at the North Rhine-Westphalia Academy of Science.